JGR Planets

RESEARCH ARTICLE
10.1029/2022JE007348

Special Section:
ExoMars Trace Gas Orbiter - One Martian Year of Science

A Two-Martian Years Survey of the Water Vapor Saturation State on Mars Based on ACS NIR/TGO Occultations

Anna Fedorova[1], Franck Montmessin[2], Alexander Trokhimovskiy[1], Mikhail Luginin[1], Oleg Korablev[1], Juan Alday[3], Denis Belyaev[1], James Holmes[3], Franck Lefevre[2], Kevin Olsen[4], Andrey Patrakeev[1], and Alexey Shakun[1]

[1]Space Research Institute (IKI) RAS, Moscow, Russia, [2]LATMOS/CNRS, Guyancourt, France, [3]The Open University, Milton Keynes, UK, [4]Department of Physics, University of Oxford, Oxford, UK

Key Points:

- Long-term observations of H_2O saturation state in the atmosphere of Mars show that supersaturation is nearly ubiquitous above aerosol layers
- During the dusty season, the supersaturation is stronger in MY35 compared to MY34
- More water was found in the evening terminator and stronger supersaturation in the morning terminator

Supporting Information:

Supporting Information may be found in the online version of this article.

Correspondence to:

A. Fedorova,
fedorova@iki.rssi.ru

Citation:

Fedorova, A., Montmessin, F., Trokhimovskiy, A., Luginin, M., Korablev, O., Alday, J., et al. (2023). A two-Martian years survey of the water vapor saturation state on Mars based on ACS NIR/TGO occultations. *Journal of Geophysical Research: Planets*, *128*, e2022JE007348. https://doi.org/10.1029/2022JE007348

Received 26 APR 2022
Accepted 5 DEC 2022

Abstract On Mars, condensation is the major factor constraining the vertical distribution of water vapor. Recent measurements of water and temperature profiles showed that water can be strongly supersaturated at and above the level where clouds form during the aphelion and perihelion seasons. Since 2018, the near-infrared spectrometer (NIR) of the Atmospheric Chemistry Suite onboard the Trace Gas Orbiter has measured H_2O and temperature profiles using solar occultation in the infrared from below 10 to 100 km of altitude. Here, we provide the first long-term monitoring of the water saturation state. The survey spans 2 Martian years from $L_s = 163°$ of MY34 to $L_s = 170°$ of MY36. We found that water is often supersaturated above aerosol layers. In the aphelion season, the water mixing ratio above 40 km in the mid-to-high latitudes was below 3 ppmv and yet is found to be supersaturated. Around the perihelion, water is also supersaturated above 60 km with a mixing ratio of 30–50 ppmv. Stronger saturation is observed during the dusty season in MY35 compared to what was observed in MY34 during the Global Dust Storm and around the perihelion. Saturation varied between the evening and morning terminators in response to temperature modulation imparted by thermal tides. Although water vapor is more abundant in the evening, colder morning temperatures induce a daily peak of saturation. This data set establishes a new paradigm for water vapor on Mars, revealing that supersaturation is nearly ubiquitous, particularly during the dust season, thereby promoting water escape on an annual average.

Plain Language Summary The rate of water loss from Mars depends on hydrogen, the main product of the H_2O photodissociation escaping from the upper atmosphere. The ability of water to reach high altitudes and to be a direct source of atomic hydrogen is limited by cloud formation, which holds water vapor in the lower atmosphere. This process is regulated by temperature and pressure. Condensation starts when the temperature is cold enough and condensation nuclei (CN) (e.g., small dust particles) are available. If CN are lacking, or their sizes are too small, or the temperature drops too fast, then water vapor becomes supersaturated. Recent studies have shown that Martian water vapor is often supersaturated. Here, we present the first seasonal cycle of the saturation state from simultaneous measurements of water and temperature during two Martian years by Atmospheric Chemistry Suite on the Trace Gas Orbiter. Our results show that supersaturation is typical on Mars. It occurs above clouds both in the aphelion and perihelion seasons as well as in the lower polar atmosphere. We demonstrate supersaturation to be an important factor facilitating the escape of water. Unlike the Earth, water easily penetrates the upper atmosphere and reaches photodissociation altitudes.

1. Introduction

The water vapor vertical distribution in the Martian atmosphere is driven by microphysics, radiative transfer, dynamics, chemistry, as well as regolith-atmosphere interaction and surface properties. Temperature is one of the main parameters controlling the saturation of water, which governs cloud formation and subsequently the vertical distribution of water. Because clouds have a radiative effect (see e.g., Navarro et al., 2014), they in turn generate a feedback loop that impacts climate overall. The cold aphelion season is characterized by a low hygropause that produces clouds and blocks water vapor below 10–20 km, thereby regulating the advection of water from the Northern to Southern Hemisphere (Clancy et al., 1996; Montmessin et al., 2004). In the warm dusty perihelion season, higher atmospheric temperatures induce a higher hygropause, with water vapor extending up to 60–80 km (Clancy et al., 1996; Fedorova et al., 2021; Montmessin et al., 2004; Trokhimovskiy, Fedorova, et al., 2015). Recent observations found that Global Dust Storms (GDS) have a strong impact on the water vertical distribution. During these events, water can reach up to 100 km, as observed during the MY28 GDS (Fedorova

et al., 2018; Heavens et al., 2018) and MY34 (Aoki et al., 2019; Belyaev et al., 2021; Fedorova et al., 2020, 2021; Villanueva et al., 2021). Such events constitute a quasi-direct source of hydrogen in the upper atmosphere, accelerating the escape of hydrogen to space (Clarke et al., 2014; Chaffin et al., 2014, 2017; Krasnopolsky, 2019; Shaposhnikov et al., 2019). In situ sampling by the Mars Atmosphere and Volatile EvolutioN (MAVEN) Neutral Gas and Ions Mass Spectrometer even showed that water molecules were propelled up to an altitude of 150 km (Stone et al., 2020), producing one of the most spectacular illustrations of the tight and fast coupling between the lower and the upper atmosphere. The link between dust and hydrogen escape was explored thanks to simultaneous measurements of dust, temperature, ice, water, and hydrogen during the regional C-storm of MY34 (L_s 310° and 320°). This isolated dust event boosted planetary H loss by a factor of 5–10 (Chaffin et al., 2021). Highly sensitive Trace Gas Orbiter (TGO) measurements were able to profile water up to 120 km during perihelion in MY34 and MY35 and during the MY34 GDS (Belyaev et al., 2021). Together with the multi-annual survey of H_2O vertical distribution by SPectroscopy for the Investigation of the Characteristics of the Atmosphere of Mars (SPICAM) (Fedorova et al., 2021), this kind of data set has proven to be insightful to address the contribution of the dusty perihelion season and that of the MY34 GDS in enhancing the production of H atoms that eventually make their way to the upper atmosphere (Belyaev et al., 2021; Montmessin et al., 2022).

Supersaturation reflects the ability of water to penetrate the cold trap associated with cloud formation and propagate above it. It also reveals an inefficient condensation process that may be attributed to a lack of condensation nuclei (CN) or higher resistance to diffusive growth. The first evidence of supersaturated water vapor in the Martian atmosphere was produced by SPICAM on the Mars Express. Maltagliati et al. (2011) observed supersaturation reaching 2 to 10 at 30–40 km in the aphelion season, from $L_s = 50°$ to 120° in both hemispheres using SPICAM water profiles and collocated Mars Climate Sounder (MCS) temperatures corrected for local time. The observed supersaturated state was then explained by possible lack of CN due to the scavenging effect; that is, a cleaning of the atmosphere of dust captured by forming ice particles and then dragged to lower altitudes by sedimentation. However, Fedorova et al., (2014) analyzing the same set of observations showed that aerosols, and thus CN were present in the atmosphere for latitudes below 60°N at 30–50 km but mostly with submicron particle size <0.1 μm. The authors estimated that the critical saturation ratio for such particles can vary from 2 to 4 for low temperatures of the middle atmosphere, in general agreement with the conclusions of Maltagliati et al. (2011). Clancy et al. (2017) used 1.27 μm $O_2(^1\Delta_g)$ dayglow profiles from the Compact Reconnaissance Imaging Spectrometer for Mars (CRISM) limb observations and the Laboratoire de Météorologie Dynamique (LMD) Mars Global Climate Model (GCM) to constrain water profiles and estimate a saturation ratio for $L_s = 60°$–140° and 200°–310° seasons. A high (>2.2) saturation ratio was found in northern mid-to-high latitudes at 20–40 km, in rough agreement with SPICAM findings. In contrast, Clancy et al. (2017) reported no supersaturation in the southern summer season, when SPICAM found supersaturation of 2–3 times at 80 km in the presence of clouds (Maltagliati et al., 2013).

However, these earlier discoveries of supersaturation had to rely on separate temperature estimates and the first simultaneous water vapor and temperature profiles were produced by Atmospheric Chemistry Suite (ACS) (Fedorova et al., 2020; Korablev et al., 2018) experiment on TGO dedicated to occultation measurements and vertical profiling of the atmosphere. TGO began its science phase in March 2018 (L_s = 163° of MY34) shortly before the GDS. ACS observed the saturation state on the global scale during the dusty season and definitely showed that supersaturation occurs even when clouds are present. Supersaturation was detected in both hemispheres above 60–80 km from $L_s = 210°$ to 340° and in high latitudes in the lower atmosphere below 20–30 km.

Poncin et al. (2022) investigated water vapor saturation in the presence or proximity of water ice clouds for co-located observations of temperature and ice clouds by MCS and water vapor profiles by CRISM and Nadir and Occultation for MArs Discovery (NOMAD) on TGO at various times during the Martian year. During the aphelion season, water was close to saturation in the presence of clouds, with the supersaturation of 2–3 at the top of the cloud layer. During the perihelion season, values of supersaturation up to 1.5 were observed in high southern latitudes near the top of the clouds. Measurements during the GDS of 2018 suggest that supersaturation did not exceed 5. Based on these measurements, a schematic model of cloud evolution was proposed (Poncin et al., 2022) with small particles formed rapidly in supersaturated regions and then growing and falling, explaining why water ice was observed even in the subsaturated region below.

Water ice clouds play a key role in the radiative transfer of the Martian atmosphere, impacting its circulation and thermal structure (Madeleine et al., 2012). Therefore, detailed cloud microphysics has become a central

component of Mars' GCMs (Haberle et al., 2019; Montmessin et al., 2004; Navarro et al., 2014; Shaposhnikov et al., 2019, 2022). The first time supersaturation was simulated by a climate model, it had to include a cloud microphysics module accounting for the nucleation of dust particles, water ice particle growth/sublimation, and scavenging (Navarro et al., 2014). The model found reasonable agreement with SPICAM observations with regard to the supersaturation level predicted above the hygropause. At L_s = 210°–240° and 330°–360° studied by the authors, temperature clearly controlled the boundary of supersaturation and its values reached 1,000 in some cases, although the absolute value of the water mixing ratio in this region was less than 1 ppmv and negligible compared to total water.

Following TGO observations, Holmes et al. (2022) studied global variations in water vapor and saturation state in the dusty season of MY34 including the GDS. Using the cloud model of Navarro et al. (2014), they assimilated observed temperature and water vapor values from a variety of instruments in the Mars' climate model. Discrete layers of supersaturated water were found at all latitudes during the dusty season of MY34. They found evidence of water supersaturation above 60 km for most of the GDS period. The GDS and the southern summer regional C-storm (L_s from 310° to 320°) forced water to be supersaturated at altitudes where it can break up and then produce hydrogen atoms that eventually escape to space. The model reanalysis indicates that it occurs at all latitudes where ACS is observed. This analysis also found evidence of water in a supersaturated state breaking into the northern winter polar vortex. The layer is centered at 20–40 km at latitudes poleward of 60°N and corresponds to cold air below the polar warming at higher latitudes. This finding has implications for the surface atmosphere exchange in the northern polar cap and water transport.

Moreover, a study by Vals et al. (2022) argues that supersaturation influences not only water transport and abundance but also the HDO/H_2O ratio. The authors used an improved global general circulation model including HDO and accounting for cloud microphysics and radiative effects. As described above, supersaturation reflects a porous hygropause (and deuteropause) allowing water to penetrate higher altitudes. It also reflects the fact that condensation is throttled down and so is HDO fractionation. In addition, supersaturation also affects the HDO condensation through kinetics effects that further reduce fractionation. D/H can subsequently be twice lower than when supersaturation is not allowed and condensation maintains water vapor at phase equilibrium.

Compared to Fedorova et al. (2020), we present here the full set water vapor saturation state obtained by the Near-InfraRed (NIR) ACS spectrometer throughout two Martian years from L_s = 163° of MY34 to L_s = 170° of MY36, while Fedorova et al. (2020) stopped their analysis at L_s = 355° of MY34. Since this first publication, the calibration of the instrument and the retrieval procedure and pipeline have been improved as described in Section 2, where an overview of the ACS NIR spectrometer, retrievals, and observation coverage is presented as well as observations of H_2O clouds with the Mid-InfraRed (MIR) channel of ACS. Section 3 provides an overview of results focusing on the seasonal, latitudinal, local time, and interannual variations. Section 4 discusses the correlation with previous measurements.

2. Observations

2.1. ACS NIR Spectrometer

TGO was launched in March 2016 and was inserted into Mars' orbit in October 2016. Routine science began in April 2018 after 18 months of aerobraking that led to the final circular 400-km orbit. ACS is a set of three high-resolution spectrometers, NIR, MIR, thermal infrared (TIRVIM) operating in the spectral range from 0.65 to 17 μm onboard TGO.

The NIR spectrometer combines an acousto-optical tunable filter (AOTF) used as a monochromator that can be commanded to isolate a specific wavelength bandpass whose width approximately corresponds to the free spectral range of the echelle grating that operates at high diffraction orders. It covers the 0.7–1.7 μm spectral range using diffraction orders 101 through 49 with a high resolving power of about 28,000 (Korablev et al., 2018; Trokhimovskiy, Korablev, et al., 2015). During an occultation, ACS NIR measures ten pre-selected diffraction orders every 2 s. Extremely high spectral resolution allows ACS NIR to sound different atmospheric constituents such as H_2O, CO, CO_2, and weak band of O_2 (Fedorova et al., 2020, 2022; Korablev et al., 2018). The duration of occultation, from 100 km tangent altitude down to the surface, varies from 1 to 4 min depending on the angle between the orbit plane and the spacecraft–Sun vector (the beta angle), which gradually changes throughout the year (Korablev et al., 2018). This results in a different number of spectra recorded during a particular

occultation (from about 30 to 130). The instantaneous field-of-view of NIR in the direction perpendicular to the limb is small (~0.02°) and limited by the slit width equal to 2 pixels. It corresponds to a vertical resolution of 500–600 m at the tangent altitude of the line of sight. The time to measure one diffraction order is 0.2 s, yielding an effective vertical resolution better than 1 km for each diffraction order. The number of detector lines measured in a single occultation and its position on the detector depends on the pointing direction (NOMAD or ACS MIR-driven) and the available downlink volume. It varies from 6 to 30 lines; the solar image size on the detector limits the upper boundary. Averaging 30 detector lines does not worsen the vertical resolution since that dimension of field-of-view is oriented along the limb. The SNR for an individual pixel and pure solar signal in the AOTF maximum is ~600 for the MIR pointing and ~300 for the NOMAD pointing.

The calibration of the ACS NIR from laboratory measurements and first in-flight data is summarized in Trokhimovskiy, Fedorova, et al. (2015) and Korablev et al. (2018). It included the AOTF characterization dependence on temperature and spectral range, signal-to-noise ratio estimations, blaze function and instrumental line shape, and resolving power variation with diffraction order and detector position. These calibrations were used in the retrievals of temperature and water vapor by Fedorova et al. (2020). The present study includes just one update, improved characterization of the AOTF profile within the diffraction order 49 to better describe the order overlapping from far sidelobes. The AOTF profile at ~1.565–1.58 μm, close to the long-wavelength bound of the detector, has not been characterized in the laboratory accurately enough and was improved using in-flight solar spectra.

The data processing of ACS NIR in occultation mode was described in Fedorova et al. (2020). The transmittance was obtained as the ratio of spectra measured inside the atmosphere to the reference solar spectrum. To obtain a reliable solar reference, we averaged spectra outside the atmosphere (above 140–150 km). We also binned 6–25 detector lines inside the solar disc with the maximal signal, excluding the solar image edges, resulting in an SNR of 800–3,000, depending on the occultation for pure solar signal. Another important modification in present data processing is the use of the recently corrected SPICE kernels by the Navigation and Ancillary Information Facility describing the spacecraft altitude. The TGO onboard clock was found to have variable bias with respect to the Universal Time Coordinated, up to several seconds at maximum, resulting in the tangent altitude prediction errors of up to several km. The geometry used here has been corrected for this anomaly.

2.2. Retrieval Algorithm

For this study, we used measurements of diffraction order 49 (6,318–6,387 cm^{-1}), order 54 (6,960–7,040 cm^{-1}), and order 56 (7,217–7,300 cm^{-1}) (Figures 1a–1d). Order 49 was initially used to retrieve the temperature and CO_2 density using the 1.57 μm CO_2 band and CO mixing ratio using a weaker overlapping band (Fedorova et al., 2020, 2022) (Figure 1b). Order 56 contains the strongest lines of the 1.38 μm water vapor band and was also used by Fedorova et al. (2020) (Figure 1d). Order 54, firstly applied here for NIR analysis, contains the strongest (in the NIR spectral range) 1.43 μm CO_2 band and weak H_2O lines on the edge of the 1.38 μm band. Together with order 49, it was used to retrieve the temperature and CO_2 density, especially at altitudes above 80 km where the 1.57 μm CO_2 band is weaker.

The retrieval follows the same methodology as the previous temperature and water vapor retrieval with this instrument (Fedorova et al., 2020). A forward model of transmission is computed using a look-up table of absorption cross-sections (as a function of pressure and temperature) for atmospheric layers determined by the number of observed target altitudes from the lowest level above the surface to ~100–120 km depending on order. For the strongest 1.43 μm CO_2 band (order 54), the maximal altitude was found to be 120 km. For the 1.57 μm band (order 49), the maximal altitude was about 100 km. The absorption cross-sections are calculated using the spectral line parameters from HITRAN 2016 (Gordon et al., 2017) with a correction coefficient of 1.7 for the H_2O broadening in CO_2-dominated atmosphere as suggested by Gamache et al. (1995), and self-broadening in the case of CO_2.

In the first step, we retrieve the temperature and pressure profiles from orders 49 and 54. The spectral resolution of NIR allows resolving the rotational structure of the CO_2 bands and disentangling weak CO features within (the CO retrievals from order 49 are described in the companion paper, Fedorova et al., 2022). The retrieval employs an algorithm proposed by Ceccherini (2005) and Ceccherini et al. (2007), which combines the Levenberg–Marquardt iterative scheme with Tikhonov regularization. Regularization is commonly employed to smooth the

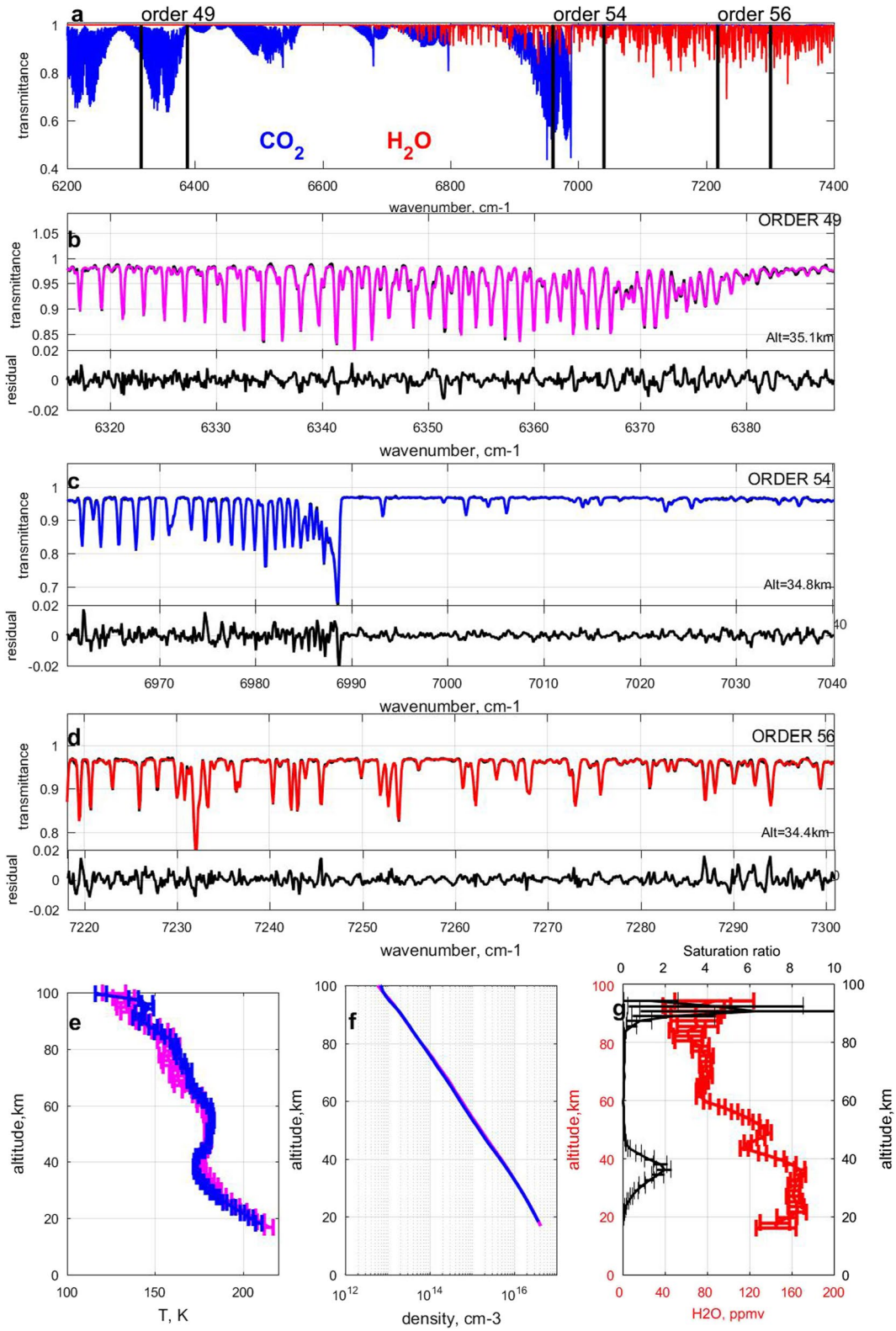

Figure 1.

profile and minimize the errors. The retrieval algorithm returns all the unknowns (temperature, pressure, and CO for order 49 and temperature, pressure, and H_2O for order 54) at all altitudes at the same time, that is, the vertical profiles (Fedorova et al., 2018, 2020) (Figure 1). However, we found that the vertical profiles of pressure retrieved from the rotational structure of the CO_2 bands sometimes generate unrealistic results. In ∼30% of profiles of the analyzed data set, we observed a bend, a drop in the pressure curve at some altitudes, contradicting the hydrostatic law. Therefore, in the second step, we assume hydrostatic equilibrium as described in Fedorova et al. (2020). We determine a pressure P_0 at an altitude level where the error is minimal in the first step (the highest data quality), and then compute the pressure profile from the hydrostatic equilibrium, integrating the retrieved T profile above and below the P_0 level. The uncertainty on the retrieved quantities on both steps is given by the covariance matrix of the solution. Results are presented in Figure 1 for temperature (Figure 1e) and density (Figure 1f) profiles. Both orders have shown very close results (see also Figure S1 in Supporting Information S1). The systematic difference between the orders 49 and 54 below 45 km does not exceed 1.5 K on average, but grows above 50 km to reach −5 K (the order 49 is colder) between 45–65 km and −8 to 9 K above 65 km. Systematics can be related to small uncertainties of AOTF calibrations and spectral resolution in the two orders as well as different absorption depths of the two CO_2 bands. To minimize these uncertainties, we use the weighted averaged profiles between two orders.

The assumption of hydrostatic equilibrium can be questioned for observations with a high beta angle, where the line of sight tracks a wide range of latitudes and longitudes. However, the occultations with a beta angle exceeding 60° constitutes ∼6% of the analyzed data set only. We also note that the difference between the rotational (T_{rot}) and the hydrostatic (T_{hs}) temperature is generally <2 K, except at low altitudes (<20 km) where the rotational temperature may be affected by the saturation of spectral lines (see Figure S2 in Supporting Information S1). For higher beta angles, the standard deviation of difference between T_{rot} and T_{hs} is growing but remains smaller than 5 K on average. We have taken into account these uncertainties as an additional 5 K systematic error for orbits with beta-angles >60°.

In the next step, the H_2O number density and v.m.r. are retrieved by applying a similar retrieval procedure (Levenberg-Marguardt combined with Tikhonov regulation) to the spectra in the diffraction order 56 (7,217–7,302 cm^{-1}). Only one free parameter vector is retrieved (the H_2O volume mixing ratio (*vmr*)) with the pressure and temperature profiles obtained in the previous step. The self-consistent retrieval of the H_2O profile, along with that of CO_2 and the temperature profile, is a more reliable approach than using the climate model predictions of temperature. These predictions are shown to have a bias compared to observations (see Fedorova et al., 2020). Figures 1b–1d show an example of spectra with the best-fit synthetic spectra, demonstrating the good quality of the data.

In the case of water vapor, the uncertainty on the retrieved quantities is also given by the covariance matrix of the solution and we account for the Jacobian errors due to the uncertainties in the retrieved T and P. For further analysis, we removed all data with H_2O uncertainties exceeding 100% or with temperature error exceeding 12 K.

ACS NIR measured CO_2 and H_2O vertical profiles together with several instruments onboard TGO. The validation of NIR temperature profiles against ACS MIR results obtained from the 2.7 μm band showed a good agreement for a wide set of simultaneous measurements (Alday et al., 2019, 2021; Belyaev et al., 2021; Fedorova et al., 2020). The water profiles were validated with the ACS MIR measurements in the 2.6 μm water band (Alday et al., 2021; Belyaev et al., 2021) and with simultaneous measurements of water vapor near 3.3 μm with NOMAD SO (Aoki et al., 2022).

2.3. Saturation Ratio

The water vapor saturation pressure depends solely on temperature in the approximation of the Clausius-Clapeyron (List, 1984), which is applicable to planetary atmospheres. For the computation of the water saturation in the

Figure 1. Example occultation spectra of CO_2 and H_2O bands measured by Atmospheric Chemistry Suite near-infrared channel and the retrieved profiles for occultation 4154 in MY34 (L_s = 278°, latitude: 55°S, longitude: 317°E, local time 3:06). (a) Synthetic spectra of CO_2 and H_2O absorptions (target altitude of 20 km); the ranges corresponding to measured diffraction orders are marked by vertical bars. (b) Observed (black) and best fit model (magenta) transmittances in order 49 at 35 km with residual. (c) Observed (black) and best fit model (blue) transmittances in order 54 at 35 km with residual. (d) Observed (black) and best fit model (red) transmittances in order 56 at 35 km with residual. Lower panels show profiles retrieved from this occultation: (e) temperature in Kelvin from orders 49 (magenta) and 54 (blue), (f) CO_2 density in cm^{-3} from the same orders and (g) water vapor mixing ratio in ppmv from order 56 with saturation ratio (black) calculated as explained in Section 2.3.

Martian atmosphere, we use a semi-empirical form of the Clausius-Clapeyron law, the Goff-Gratch equation (Goff & Gratch, 1946) that yields the vapor pressure over ice:

$$\log P_{\text{sat}} = 2.07023 - 0.00320991\,T - 2,484.896\,T^{-1} + 3.56654 \log T,$$

where P_{sat} is the saturation vapor pressure in mbar, and T is the temperature in kelvin. The choice of saturation equation can be critical for low temperatures typical of the Martian atmosphere. The Goff-Gratch equation was recommended for temperatures from −100°C to 0°C. The comparison with recent accurate formulas from Wagner et al. (2011) and Huang (2018) has shown an agreement inside 0.25% of pressure for temperature as low as 155 K and inside 4% for 120 K, to be compared with the factor of two changes induced by the uncertainty of about 5 K.

The saturation ratio S is defined as $S = P_{\text{H2O}}/P_{\text{sat}}$. The uncertainties of S are evaluated as the total differential of S, using the uncertainties of the retrieved temperature, pressure, and water *vmr*.

2.4. Aerosol Loading Estimation

To complete the water vapor and temperature profile extraction, the aerosol extinction can also be retrieved. ACS NIR measures the atmospheric extinction in all diffraction orders used during an occultation. Two orders are dedicated only to measuring aerosols: order 78 around 0.99 μm (10,052–10,170 cm^{-1}) and order 90 around 0.86 μm (11,500–11,734 cm^{-1}). When measuring CO_2 and H_2O using orders 49, 54, and 56, aerosols can be retrieved from the continuum in between the gaseous absorption bands. From NIR spectra, it is not possible to distinguish between dust and water ice aerosols; thus, NIR extinctions should be treated as a product of both types of aerosols.

To distinguish water ice cloud particles, in addition to NIR, we also used aerosol extinction retrieved from ACS MIR occultation data. This procedure has been described in detail and validated in Fedorova et al. (2020) and the related Supporting Information.

First, we apply a standard "onion peeling" method (Rodgers, 2000) to retrieve vertical profiles of aerosol extinction and associated uncertainties from the ACS solar occultation data for NIR and MIR independently (Fedorova et al., 2009, 2014, 2020). From NIR data, extinction is retrieved from orders 49 (6,318–6,387 cm^{-1}), 56 (7,217–7,300 cm^{-1}), 78 (10,052–10,170 cm^{-1}), 90 (11,500–11,734 cm^{-1}), and 101 (13,016–13,170 cm^{-1}), following Luginin et al. (2020). From MIR data, we use spectra measured in the secondary grating position 12 (2,905−3,265 cm^{-1}), which includes a water ice absorption band at ∼3 μm (Fedorova et al., 2020; Stcherbinine et al., 2020).

MIR aerosol extinction at the center of the water ice band (3,225 cm^{-1}) is treated as a substitute for aerosol mass loading, and extinction at several other wavelengths allows distinguishing between water ice and dust particles. Specifically, the ratio between MIR extinction at 3,225 cm^{-1} and NIR extinction at 10,126 cm^{-1} is used to estimate particle size, while the ratio between MIR extinctions at the center (3,225 cm^{-1}) and the wing (2,922 cm^{-1}) of the water ice band defines the aerosol type (for more details, readers are referred to Table S2 in Supporting Information of Fedorova et al., 2020). In this work, we used MIR aerosol extinction at 3,225 cm^{-1}, which was attributed to water ice, as a proxy for water ice mass loading.

From April 2018 to January 2022, ACS MIR performed 866 solar occultation measurements in the secondary grating position 12, almost ten times less frequent than the NIR channel. Figure 2 shows a comparison of MIR extinction at 3,225 cm^{-1}, produced by water ice particles with blue color showing the part of extinction satisfying water ice criteria, with one of NIR extinction at 1.4 μm for two example observations: 5987_E at L_s 2° of MY 35 at low latitudes, and 12756_I at L_s 289° of MY 35 at high latitudes. To validate the extinction relation method, Figure 2 also contains water ice mass loading retrieved from a complex solution of the inverse problem from the simultaneously recorded MIR and NIR spectra with a procedure described in Luginin et al. (2020).

2.5. Data Set

TGO performs an occultation on each node of the 2-hr orbit with one or both of the two instruments: ACS and NOMAD. Because of a subtle misalignment of the ACS and NOMAD lines-of-sight, two occultation observing modes are implemented: ACS MIR-driven and NOMAD-driven. ACS NIR operates both kinds of pointing, but ACS MIR can be used only with the ACS pointing. On average, ACS NIR accomplished seven occultations per

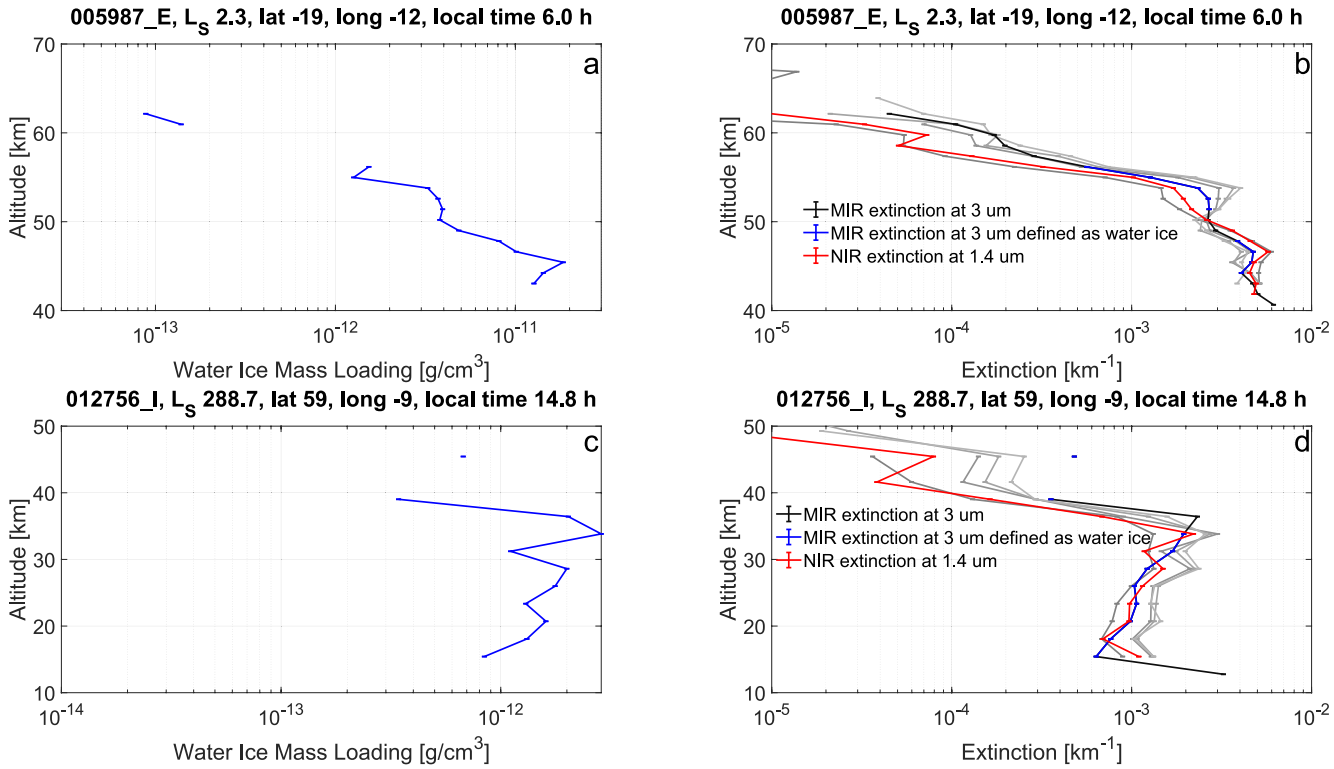

Figure 2. Aerosol loading estimation for observation 5987_E at L_s 2° of MY 35 (top panels), and 12756_I at L_s 289° of MY 35 (bottom panels). Retrieved water ice mass loading (a and c); MIR aerosol extinction at 3,225 cm^{-1}, which was attributed to water ice (blue lines at panels (b and d)); near-infrared (NIR) aerosol extinction at 1.4 μm (red lines at panels (b and d)). Black lines at panels (b and d) correspond to mid-infrared aerosol extinction at 3,225 cm^{-1}, not attributed to water ice particles. Gray lines from light to dark at panels (b and d) correspond to NIR aerosol extinctions 13,000 cm^{-1} (0.76 μm) and 7,250 cm^{-1} (1.57 μm).

sol in both hemispheres (from 1 to 21) except during several periods of about 15–20 days without occultations due to orbital plane orientation. ACS NIR provides water vapor in the 1.38 μm band and temperature measurements in 1.57 and 1.43 μm CO_2 bands, as well as aerosol extinctions at various wavelengths for each occultation. We analyzed NIR occultation profiles obtained with both ACS and NOMAD pointings (the latter constituting ~40% of profiles). From the beginning of the TGO science phase in April 2018 (L_s = 163° of MY34) to January 2022 (L_s = 170° of MY36), ACS NIR collected ~8 500 profiles (Figure 3).

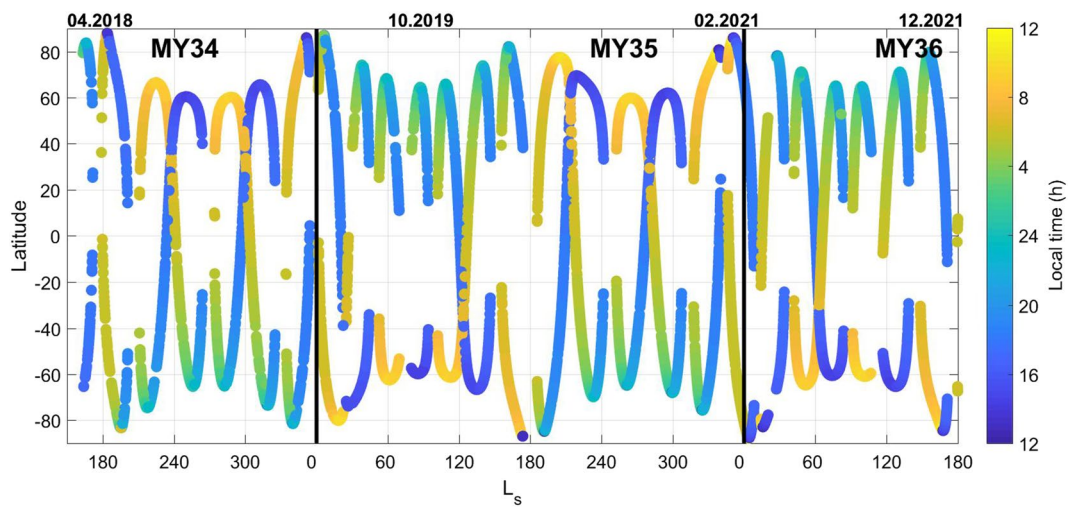

Figure 3. Observational coverage of Atmospheric Chemistry Suite near-infrared solar occultations for MY34-36 from April 2018 to January 2022. Colors indicate the local time of the occultation.

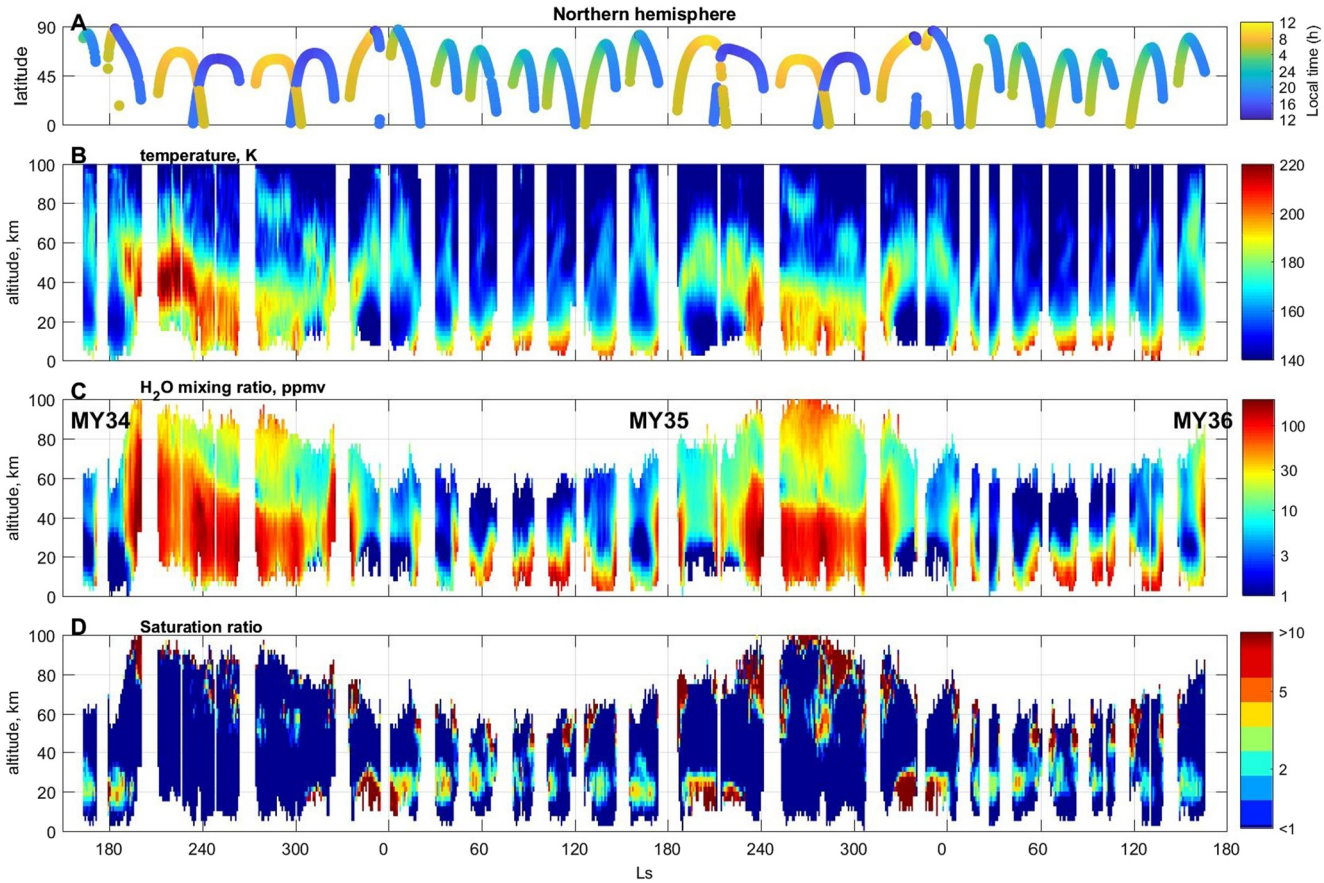

Figure 4. Seasonal variation in temperature (b), water vapor (c), and saturation ratio (d) profiles from L_s = 163° of MY34 to L_s = 170° of MY36 retrieved from the Atmospheric Chemistry Suite near-infrared data in the Northern Hemisphere. The retrieval was binned into intervals of 1° L_s and 2 km altitude. The panel (a) shows the latitudes and local time of the measurements.

3. Results

3.1. Seasonal Variations

Figures 4 and 5 show the seasonal variations in temperature, water vapor, and saturation ratio in both hemispheres extracted from our data set. The map exhibits the well-known imprint of seasons on temperature and water that far exceeds variations due to latitudinal sampling. The first strong increase in water vapor in the atmosphere corresponds to the GDS of 2018 that began shortly after L_s = 193° and was studied in detail in Aoki et al., 2019; Belyaev et al., 2021; and Fedorova et al., 2020. Both hemispheres show a sharp temperature rise of up to 220 K below 60 km (Figures 4b and 5b). The water mixing ratio in the northern hemisphere exceeds 100 ppmv below 80 km and stays at 50 ppmv up to 100 km (Figure 4c). Such a strong increase in water was never observed again after MY34 and later during the entire MY35. The second strong increase in water at high altitudes corresponds to L_s = 240°–300° and is related to the perihelion near the southern summer solstice when the Hadley circulation cell brings water from the wetter Southern Hemisphere to the Northern Hemisphere (Houben et al., 1997; Montmessin et al., 2004; Richardson and Wilson, 2002a, 2002b). At that season, southern water exceeds 50 ppmv at all altitudes below 100 km and 200 ppmv below 60 km (Figure 5c). In contrast, in the Northern Hemisphere, two layers of water were observed: (a) a lower layer containing more than 100 ppmv from the lowest observable altitude up to 40–50 km followed by a sharp decrease to 10–20 ppmv between 50 and 70 km and (b) a higher layer marked by an increase up to 30–50 ppmv from 70 to >90 km. This high-altitude water layer observed both in MY34 and 35 in the upper atmosphere illustrates the strength of water transport during that part of the year.

A regional "C-storm" occurred in MY34 between L_s 315° and 330°. This type of dust event was studied in detail, combining observations and models to illuminate the water escape in these particular climatic conditions

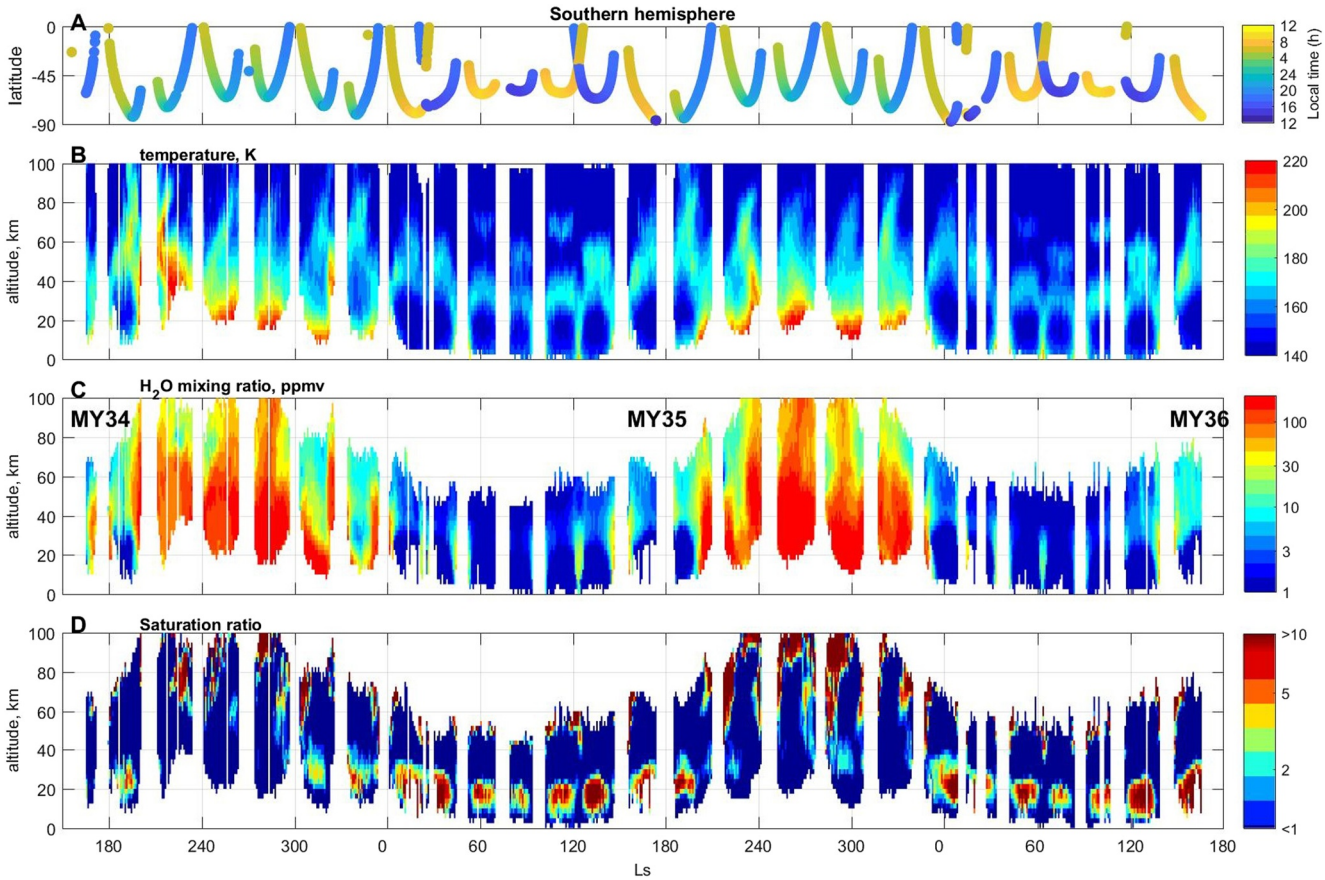

Figure 5. Same as Figure 4, except for the Southern Hemisphere.

(Chaffin et al., 2021; Holmes et al., 2021; Stone et al., 2020). The intensity of this event varies from year to year (Kass et al., 2016). Another C-storm in the ACS data occurred in MY35, although a little earlier (~10°) in the season when water in the Southern Hemisphere was carried up to 80 km.

Around the aphelion, the equatorial region meets its coldest time, leading to a strong decrease in the hygropause and water lines were not observed above 60 km. In the Northern Hemisphere, a water maximum of 200 ppmv was observed below 20–30 km, with the hygropause increasing its altitude from high to low latitudes. Above these altitudes, water sharply decreases to 1–5 ppmv, which was observed both in MY35 and in MY36 and was well correlated with the decrease in temperature from 200 to 160 K (Figures 4b and 4c). In the Southern Hemisphere, water vapor was also observed up to 60 km, but the typical values rarely exceeded 1–3 ppmv except close to the equator, where values were found to reach 20 ppmv (Figure 5c). At that season (L_s = 30°–150°) in the middle latitudes, the atmosphere near 30–40 km is characterized by a warm layer associated with water abundance of 3–5 ppmv. This layer is produced by transport from the Northern Hemisphere. In the cold lower atmosphere, the temperature does not exceed 160 K and water remains mostly below 1 ppmv. Yet, water lines are still visible, and a high supersaturation was confidently inferred.

3.2. Aphelion Season

Figure 6 presents the latitudinal variations in temperature, water vapor, saturation ratio, aerosols, and H_2O ice extinction from L_s = 0° to 180° for MY35 and MY36. Shortly after the northern vernal equinox (L_s = 0°–30°), temperature, and water are distributed almost symmetrically about the equator, with a warm region of 180 K between 30°S and 40°N from the surface up to 40 km (Figure 6a). The picture is very close for both years despite the difference in latitude coverage. In the mid-to-high latitudes, warm layers of about 180 K were observed in both hemispheres at 40–60 km, correlating with the prominent (~10 ppmv) branch of water (Figure 6b),

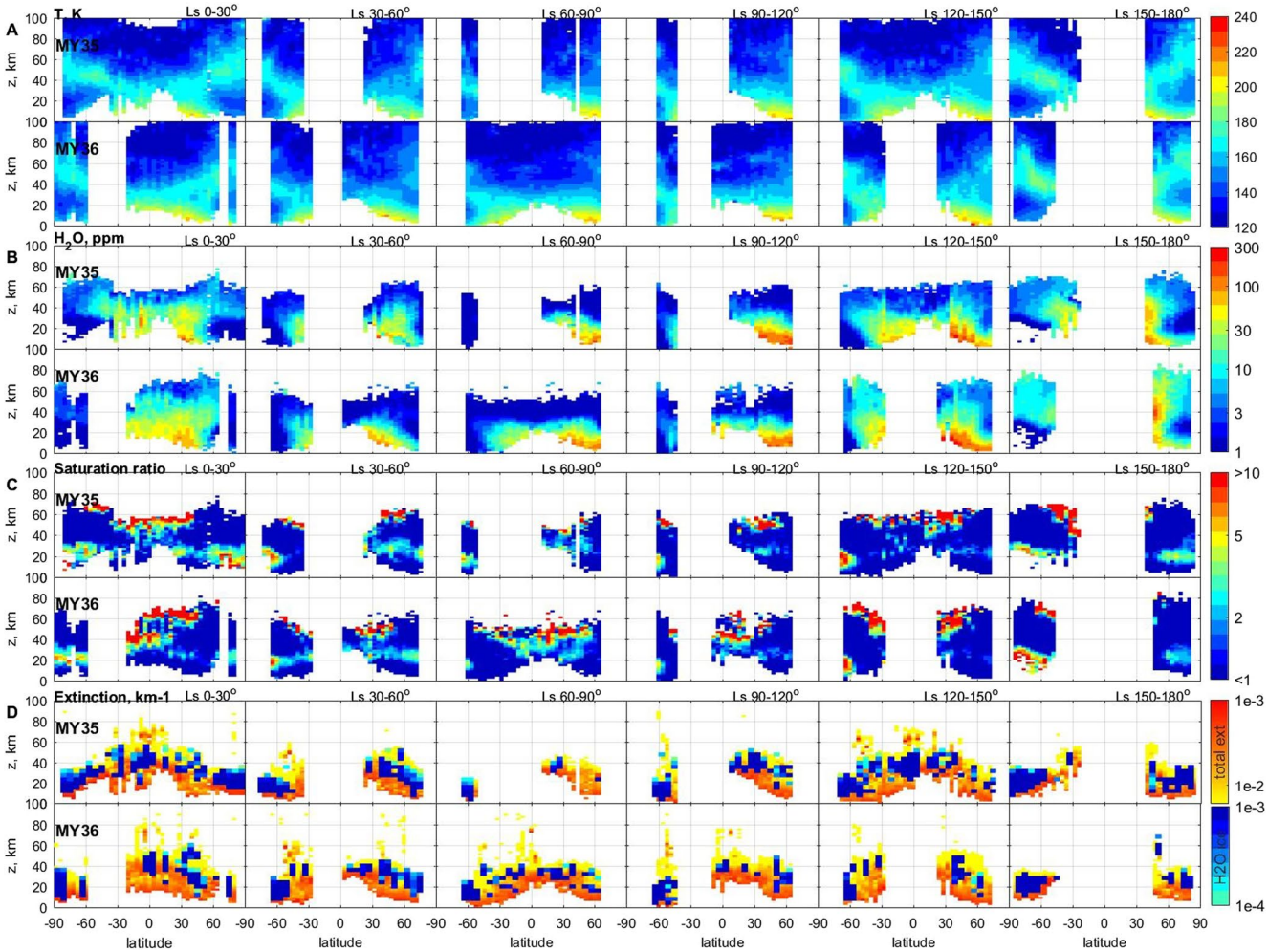

Figure 6. Latitudinal variation in temperature (a), water vapor (b), saturation ratio (c), and aerosol extinction, yellow—red dust, shades of blue—water ice clouds, (d) vertical profiles in the aphelion season from $L_s = 0°$ to 180° for MY35 and MY36. The retrievals are binned in 30° of L_s with an interval of 1° of latitude and 2 km of altitude.

which is a consequence of the transport of water from the equatorial region to high latitudes. Below these warm layers, the temperature minima are observed near the poles named "polar vortex" (Heavens et al., 2011) where water abundances decrease abruptly to the sub-ppm level. Downwelling water starts to be strongly supersaturated (Figure 6c) with clouds' forming (Figure 6d) in this polar region in MY35 and MY36 in the South and only in MY35 in the North. In the North, saturation ratios of only <3 were detected. The difference in this region between MY35 and MY36 is related to the temporal coverage of occultations. In MY35, occultation measurements occurred during the $L_s = 0°–10°$ timeframe, but in MY36 they occurred between 20° and 30° at a time when the atmosphere is becoming warmer (Figure 6a). The second supersaturated area is located at low-to-mid latitudes. There, the lowest supersaturated altitude is found around 40 km near the equator and at 55–60 km at 40°S and 45°N of latitude (Figure 6c). This saturation layer is located above the cloud formation region that is lofted below 40 km (Figure 6d). The cloud level marks a sharp decrease in water from 50 ppmv to 3–5 ppmv as a result of condensation.

From the equinox to the solstice, the near-surface temperature and water maxima grow and shift to the middle ($L_s = 30°–60°$) and high ($L_s = 60°–90°$ and 90°–120°) northern latitudes (Figures 6a and 6b). In these areas, water is always far from saturation. In the Southern Hemisphere, at $L_s = 30°–60°$, 30–50 ppmv of water is still observed near the surface in the mid-latitudes. At higher altitude (~40 km) of the high latitudes, a drier layer of water of about 3 ppmv persists and is associated with large supersaturation above 50 km where almost no aerosol is observed (Figures 6c and 6d). In the southern polar latitudes below 20 km, water also begins to be

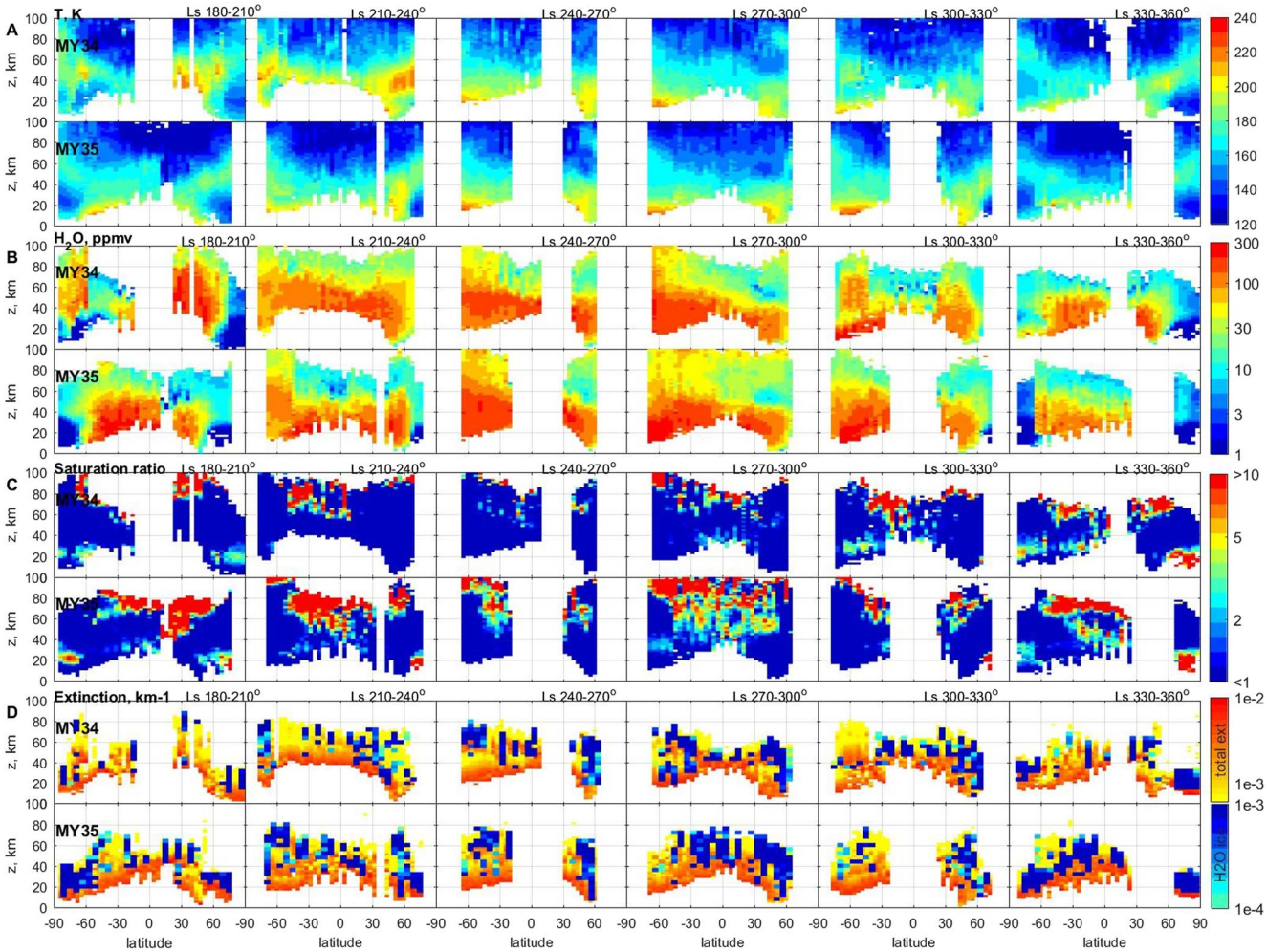

Figure 7. Latitudinal variation of temperature (a), water vapor (b), saturation ratio (c), and aerosol extinctions, yellow-red—dust, shades of blue—water ice clouds (d) vertical profiles in the perihelion season from L_s = 180° to 360° for MY34 and MY35. The retrievals are binned in 30° of L_s, with an interval of 1° of solar longitude and 2 km of altitude.

supersaturated despite the drier sub-ppm conditions. At L_s = 60°–90° and 90°–120° from middle southern to middle northern latitudes, the water decreases above the cloud region at 35–40 km from 30 to 50 ppmv to <1–2 ppmv. Once again, water above the cloud-level layer is found to be highly supersaturated (Figures 6a–6c).

Closer to the autumn equinox, the L_s = 120°–150° and 150°–180° intervals show a shift of the water peak to the equator again following the onset of the equinoctial circulation pattern, characterized by two cells facing each other around the equator. However, no strong supersaturation was observed below 20 km in the northern polar region due to warmer temperatures compared with the southern polar region.

3.3. Perihelion Season

Figure 7 shows the same latitudinal variations in temperature, water vapor, saturation ratio, and aerosol extinction as Figure 6 except for the perihelion season from L_s = 180°–360°, in 30° L_s bins for MY34 and 35.

MY 34 was characterized by the GDS that began at L_s = 193° and vanished around L_s = 240°. It can be seen as a strong interannual variability between MY34 and MY35 from L_s 180° to 240°. During MY35, water is distributed from 60°S to 45°N with values of 200 ppmv found in the South up to 60 km, above which water decreases to 30 ppmv at 80 km. In the North, these high abundances are only seen up to 40 km. The atmospheric layer where most of the decrease occurs is well correlated with aerosol extinction and temperature. This period of time

corresponded to the onset of large supersaturations. Close to the poles, the water layers located at 40–70 km appear to be correlated with warm temperatures and are likely the result of advection. Below 40 km, downwelling water exhibits supersaturation and cloud formation at low temperatures. As reported in other studies (Kass et al., 2020; Neary et al., 2020), the MY34 GDS warmed the atmosphere as captured by ACS in the North (Figure 7a) where the temperature below 60 km is 30–40 K warmer than in MY35. In the southern hemisphere, the region between 10° and 60°S was observed before GDS, whereas the region between 60° and 90°S could only be observed after it started (Figure 3). This period is characterized by water observed up to 80 km with values of >100 ppmv, which sharply decreases to 30–50 ppmv above 100 km (Belyaev et al., 2021). At this season in MY34, water begins to be supersaturated only above 70–80 km where clouds actually form (Fedorova et al., 2020; Liuzzi et al., 2020; Luginin et al., 2020; Stcherbinine et al., 2020). At L_s = 210°–240°, the atmosphere is much warmer than in MY35. Water mixing ratios up to 100 ppmv were observed at high altitudes that are above 70 km in high southern latitudes and above 60 km in high northern latitudes. In both cases, water is again observed to fall rapidly down to a mixing ratio of 30 ppm. At these high altitudes, water is supersaturated, yet aerosols are present up to 80 km, indicating that cloud or aerosol presence was not sufficient to relax the atmosphere to saturation. In MY35 between 45°S and 60°N, water is again strongly supersaturated up to 40 km even in the presence of aerosols. At 70°–50°S, the water maximum is pushed higher up to 80–100 km, which may actually be the consequence of the set-up of the solstitial circulation (Montmessin et al., 2004; Richardson and Wilson, 2002a, 2002b).

During the southern summer solstice (L_s = 240°–270° and 270°–300°), the water distribution is very similar for two years with asymmetry between hemispheres also observed by SPICAM/MEx (Fedorova et al., 2021). In the mid-to-high southern latitudes, 200 ppmv are observed up to 60–70 km. This water top gradually decreases to 40 km in the northern hemisphere at 60°N. At these altitudes, clouds are observed for both years from 60°S to 60°N. At 30°–70°S above 70 km, the water abundance sharply decreases to 50–70 ppmv and reaches 100 km and higher. In the Northern Hemisphere, H_2O decreases to 10–30 ppmv between 40 and 80 km and then increases again, revealing the transport of water from the southern to the Northern Hemisphere at high altitudes. Water is strongly supersaturated during this season for both years. But saturation is much higher for MY35 compared to MY34 and begins above 40 km near the equator and above 70 km at high latitudes. Moving to the northern vernal equinox, circulation is shaping a nearly symmetric picture that is observed for both years. The regional dust storm "C" happened between L_s = 315° and 330°, whose effect can be grasped in the L_s = 300°–330° interval in the form of a rise in the water mixing ratio and aerosol extinctions up to 70–80 km in the 45°–70°S region. In both years, supersaturation was observed at high altitudes with a water mixing ratio of about 30 ppmv. At L_s = 330°–360° in high southern polar latitudes below 20 km, supersaturation reappears despite the sub-ppmv concentration. A simple interpretation points to the local cooling of the polar atmosphere as water is still present and condensation is unable to keep up with the fast temperature decrease.

3.4. Local Time Variations

Diurnal temperature variations in the Martian atmosphere have been observed by many spacecraft such as TES/MGS, MCS/MRO, PFS/MEX, and ACS TIRVIM/TGO (Giuranna et al., 2021; Guerlet et al., 2022; Heavens et al., 2011; Kleinböhl et al., 2013; Wilson, 2000). These data have allowed the study of thermal tides driven by diurnal solar forcing (Forbes et al., 2020). Thermal tides dominate the daily temperature cycle over most of the atmospheric column. Along with diurnal tides, semi-diurnal tides dominate the temperature structure of the middle atmosphere throughout the year from high to low latitudes (Kleinböhl et al., 2013). The morning to evening difference in temperature should therefore also impact water vapor and ice, as they are captured by ACS occultations at both terminators.

The saturation state should also be sensitive to the presence of dust as CN in the atmosphere. Observations by PFS have revealed local time variations of dust opacity in the atmosphere. Wolkenberg and Giuranna (2021) have found that aphelion dust opacities are minimum at night and early morning, with perceptible variations during the rest of the day. During the dusty season, no local time variation was found (Giuranna et al., 2021). Diurnal variation of dust was also found during the GDS of MY34 by the MCS (Kleinböhl et al., 2020) when dust was found at the highest altitudes in the late afternoon and at the lowest altitudes late at night. In addition, the dust diurnal cycle was observed to vary with latitude.

The ACS data set allows us to study the local time variations of water vapor by comparing occultation measurements in the morning and evening terminators. Typically, measurements of sunset and sunrise belong to different

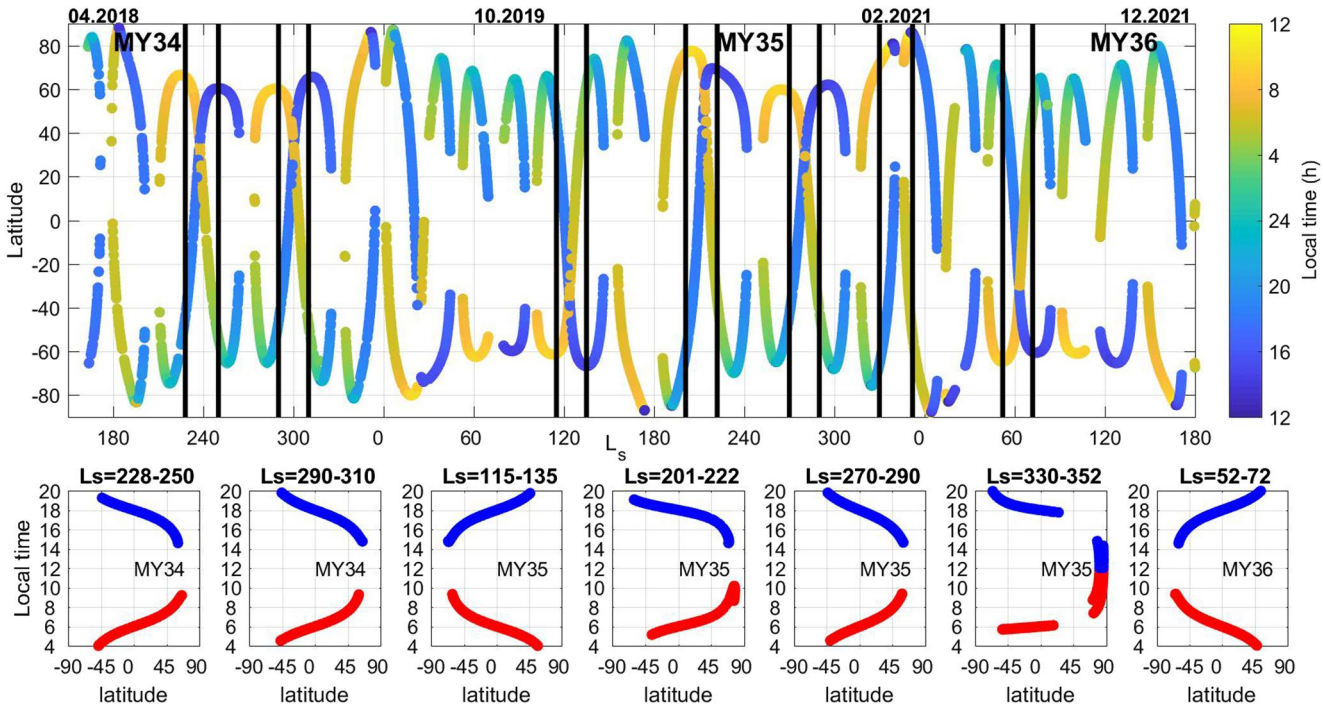

Figure 8. The latitudinal distribution of Atmospheric Chemistry Suite near-infrared occultations with ranges selected for the search of local time variations (black vertical lines). Bottom panels: zoom at local time inside the indicated bins with red curves for morning terminator and blue curves for evening terminator.

hemispheres, precluding a meaningful comparison of their respective atmospheric states. However, from time to time, a range of close latitudes was probed in the morning and evening terminators within short L_s intervals (Figure 8). To examine the morning to evening contrasts, we chose seven intervals: two in MY34 (230°–250° and 290°–310°); four in MY35 (115°–135°, 200°–220°, 270°–290°, and 330°–350°), and one in MY36 (50°–70°). Within each bin, the local time varies along the latitude (see Figure 8, bottom panels).

Figure 9 presents a latitude-altitude cross-section of temperature and water vapor in morning and evening terminators with the difference between them. A typical signature of thermal tides is prominent in the difference, with negative and positive temperature differences alternating along the vertical and stretching horizontally along latitudes (Forbes et al., 2020; Haberle et al., 1999; Zurek, 1976). Two bins around the aphelion, one in MY35 after solstice L_s = 115°–135° and one in MY36 before solstice, L_s = 50°–70° reveal positive differences at 40 and 80 km and negative differences at 60 km in low latitudes where sampled local times correspond to 06:00 a.m. and 06:00 p.m. (Figure 8). These patterns are reminiscent of MCS/MRO observations (Kleinböhl et al., 2013) and ACS TIRVIM/TGO (Guerlet et al., 2022). At 45°S and 45°N, there is a flip of sign in the temperature difference. There, the temperature difference exceeds 20 K. During these seasonal bins, water vapor mixing ratios were below 3–5 ppmv between 40 and 60 km, and from 10 to 200 ppmv below 40 km at low-to-mid latitudes. Despite the warm temperature anomaly observed at the morning terminator at 60 km in the equatorial region, water is located mostly below. At 40 km, the temperature was warmer in the evening by 20–25 K, and we observed more saturation in the morning. In the lower atmosphere, more water was observed in the evening below 30 km in the middle northern latitude where 5–10 K warmer temperatures were measured.

During the dusty season (at L_s = 200°–220° and 270°–290° of MY35), the evening temperature was warmer by 20–30 K from 30°S to 30°N at altitudes ranging from 40 to 65 km. This maximum is correlated with a low saturation ratio in the evening (~1–2) compared to strong supersaturation in the morning. Water distribution also varies with local time. At L_s = 200°–220°, water abundance increases by 10–40 ppmv in the evening at all altitudes. From L_s 270° to 290°, more water is observed in the evening between the equator and 45°S. This morning-to-evening increase might be attributed to an intensification of the mean upward motion during the daytime. A similar configuration has also been seen during L_s 230°–250° of MY35 before the solstice.

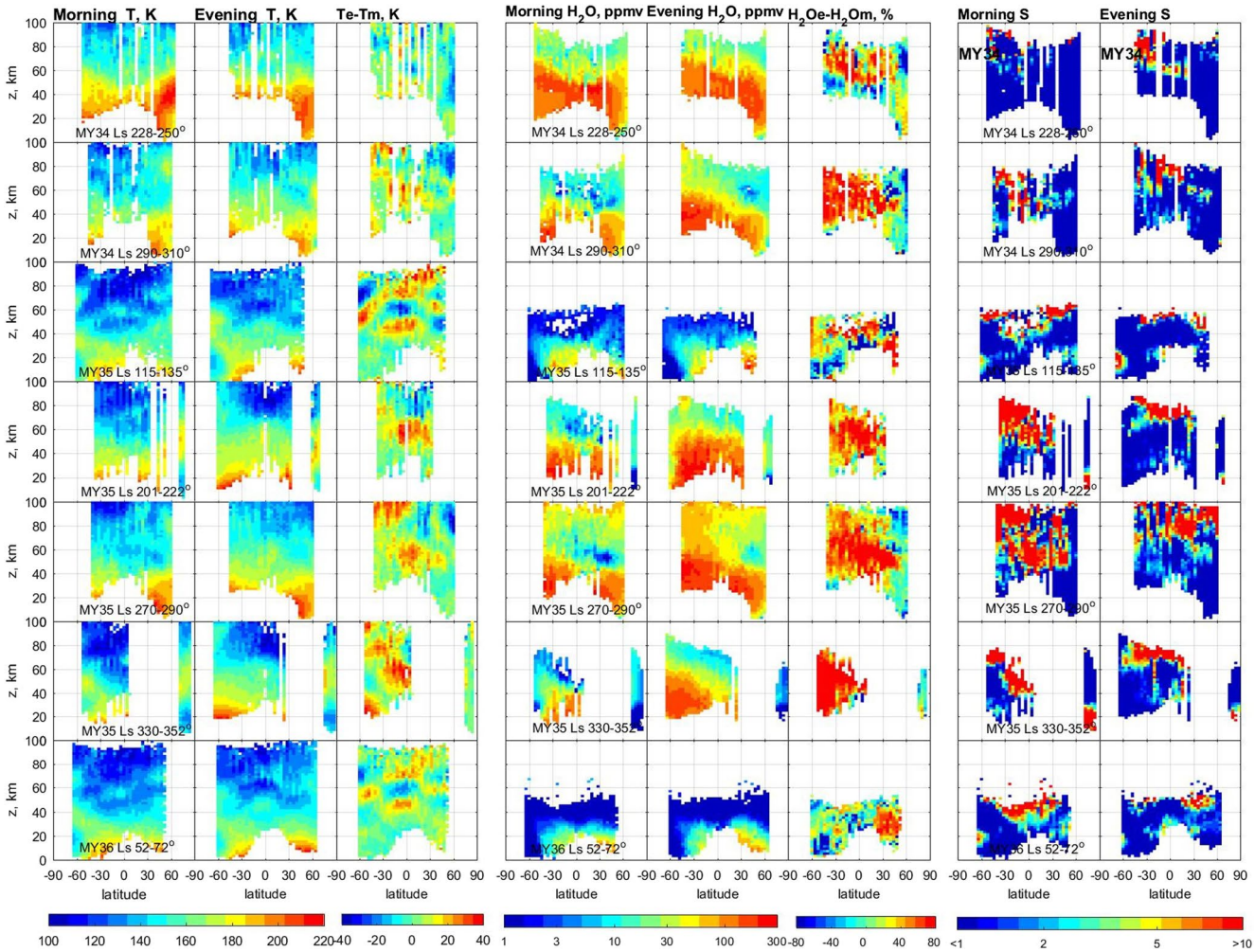

Figure 9. Morning to evening temperature contrast, water vapor and saturation ratio vertical profiles in the selected seasonal bins, from top to bottom: MY34, L_s = 228°–250°, 290°–310°; MY35: L_s = 115°–135°, 201°–222°, 270°–290°, 330°–352°; and MY36: L_s = 52°–72°. From left to right: morning, evening, and differences in temperature in K (left), water vapor mixing ratio in ppmv and difference in percent (center), morning and evening saturation ratio S (right).

Close to the northern vernal equinox (330°–350°) of MY35, the warmer temperature prevailing from 40 to 60 km in the low-to-mid southern latitudes in the evening also raises the saturation altitude by 20 km compared to the morning, with water vapor mixing ratio being higher by 10–30 ppmv compared to the morning.

3.5. Longitudinal Variations

The solar occultation measurements are not appropriate to study longitudinal distribution, but the good statistics of ACS-NIR allowed us to construct such maps at least for some special locations. Figure 10 shows longitudinal cross-sections of temperature, water vapor, and saturation state for narrow latitude bands from 55° to 60° of northern latitudes around the middle of northern winter L_s = 255°–295° of MY 34 and 35. Both in MY34 and MY35, the temperature has shown a minimum near 60 km and a maximum near about 80 km with prominent longitudinal variations. At 60–80 km, there are prominent minima of temperature at East longitudes from 0° to 30° and from −150° to −90° that can reflect the propagation of tides and planetary waves in the middle atmosphere (Wu et al., 2015). We do not try here to identify the wave activity in the Martian atmosphere. We would like to show that water and saturation state longitude-altitude distributions are well correlated with temperature wave propagation in the atmosphere. The H_2O mixing ratio has two minima between 50 and 80 km corresponding to temperature minima. This wave activity is also reflected in the saturation state of water when the supersaturation is observed only in the region with the lowest temperature and has prominent longitude variations.

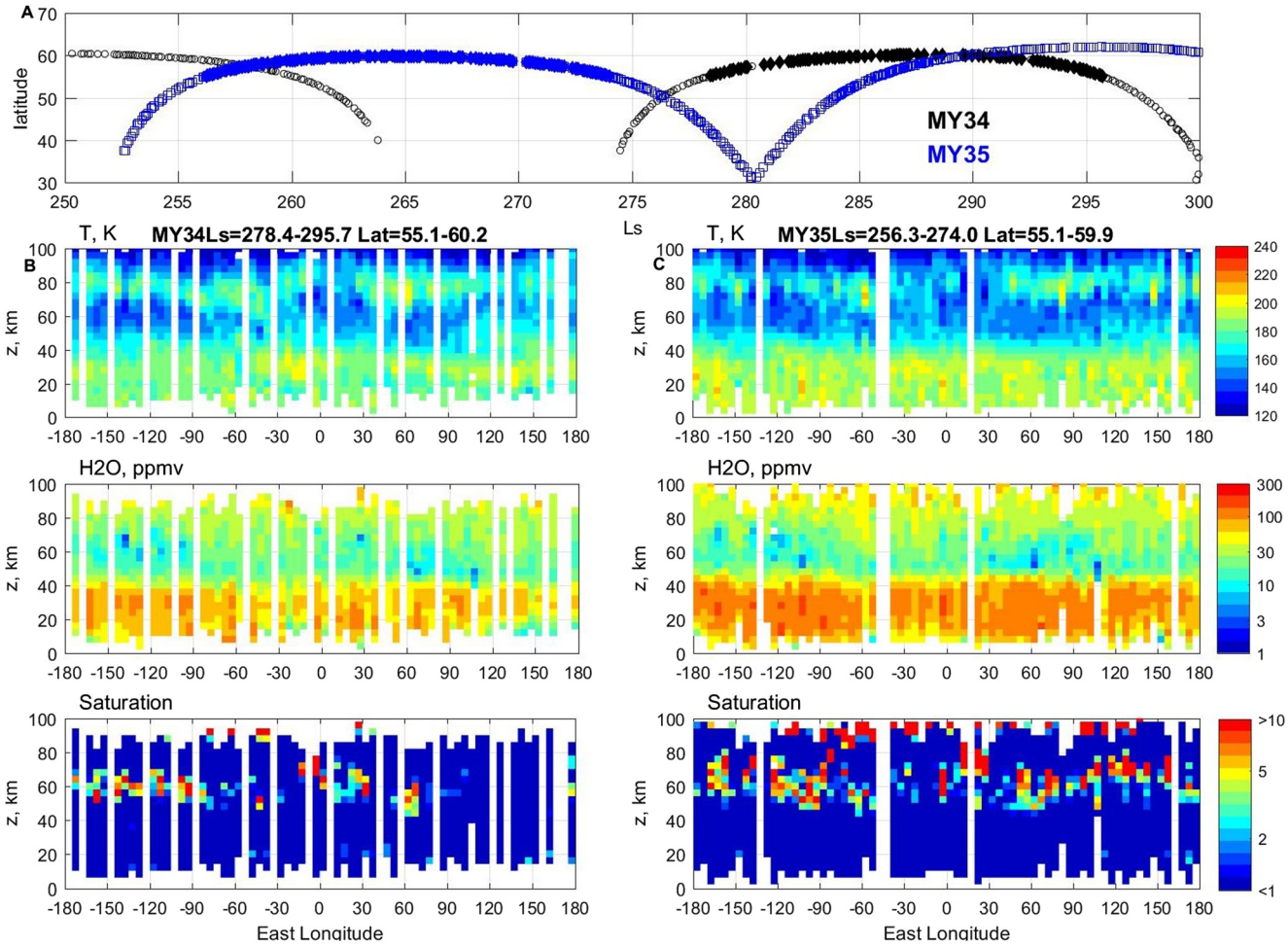

Figure 10. The longitudinal cross-sections of temperature, water vapor and saturation ratio vertical distribution for two selected areas in MY34 and MY35 in middle northern latitudes between 55° and 60°N during the northern winter. (a) Latitudinal-seasonal distribution of Atmospheric Chemistry Suite near-infrared observations with selected occultations marked as large diamonds, black color for MY34 and blue color for MY35. (b) Observations for MY34 at L_s = 278°–295°; and (c) observations for MY35 at L_s = 256°–274°.

4. Discussion

The first evidence of water supersaturation in the Martian atmosphere was obtained during the aphelion season (from L_s 50° to 120°) from SPICAM solar occultations in MY29, when 61 water vapor vertical profiles were retrieved and reported by Maltagliati et al. (2011). Lacking simultaneous temperature measurements, SPICAM saturation ratios relied on nearly-simultaneous MCS/MRO temperature profiles, with a GCM-based correction applied to compensate for the difference in local time between the two instruments. Sixty percent of the data showed water vapor exceeding saturation and more than 10% the saturation ratios greater than 5. Later, (Clancy et al., 2017) derived a proxy of water profiles by scaling LMD GCM simulated water vapor by the ratio of LMD simulated to CRISM retrieved 1.27 μm $O_2(^1\Delta_g)$ dayglow vertical emission rate. Using the GCM simulated temperature, the saturation ratio was then averaged during the L_s 60° to 140° period. They obtained saturation ratios >2.2 at northern mid-to-high latitudes between 20 and 35 km, which is roughly consistent with the SPICAM supersaturation measurements in Maltagliati et al. (2011).

Figure 11 presents the comparison of SPICAM IR observations of water vapor and saturation ratio at L_s = 75°–100° with ACS NIR observations in MY35 and 36. Latitudinal coverage of SPICAM and ACS NIR is shown in Figure 11a. In MY34 ACS NIR performed measurements at the same latitudes as SPICAM between L_s = 80° and 94°, whereas in MY35 the observations are closer before L_s = 83° and after L_s = 92°. Despite the coarser vertical resolution of SPICAM IR (1–10 km for SPICAM and <1 km for NIR) and a lower SNR (~100 for SPICAM and

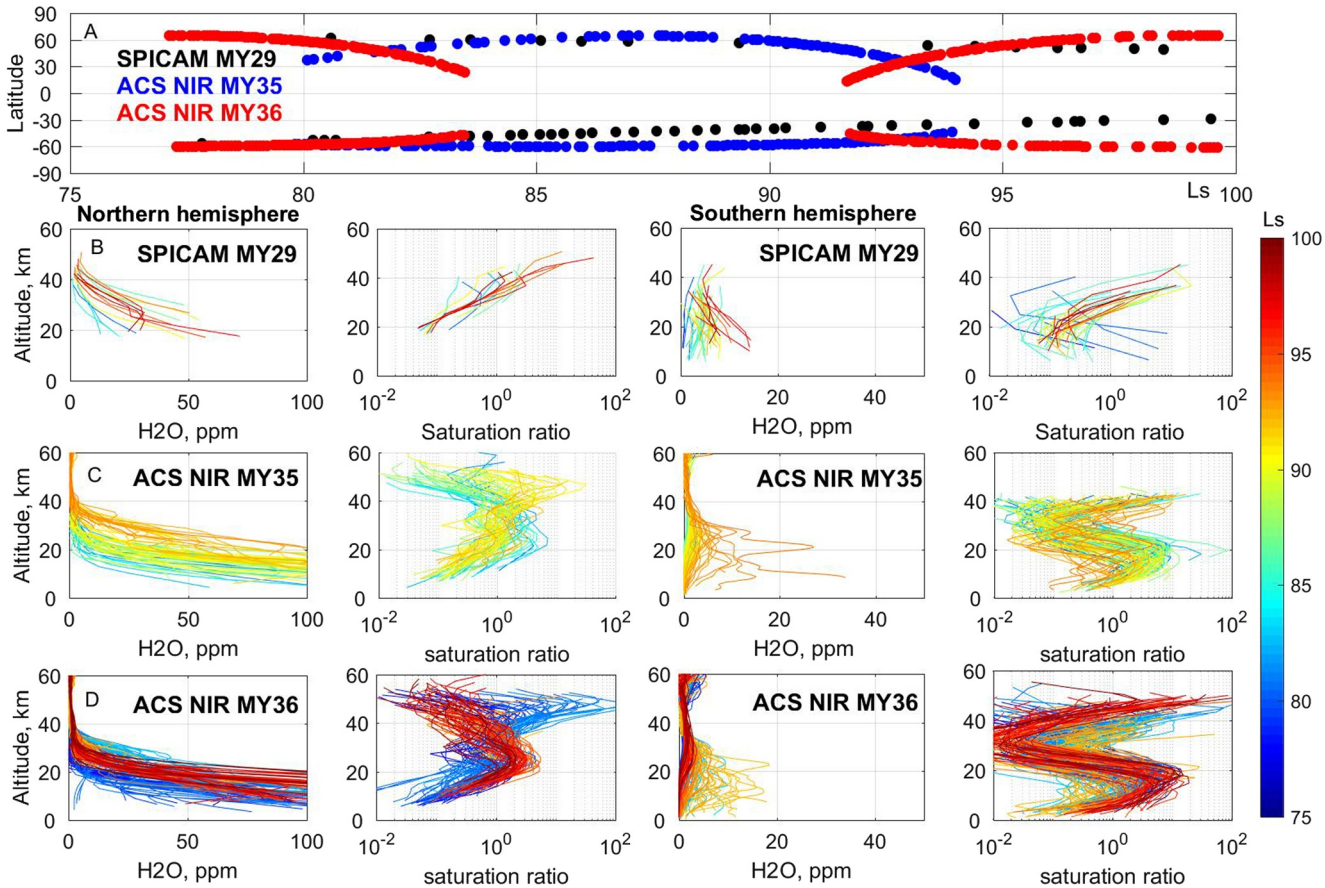

Figure 11. Water vapor vertical profiles and saturation ratio obtained from SPectroscopy for the Investigation of the Characteristics of the Atmosphere of Mars (SPICAM) IR occultations in MY29 (b) and Atmospheric Chemistry Suite (ACS) near-infrared (NIR) observations in MY35 (c) and MY36 (d) at $L_s = 75°–100°$ in the northern and southern hemispheres. Panel (a) presents the latitudinal coverage of occultations.

~1,000 for NIR), the water vapor vertical profiles of SPICAM (Figure 11b) are consistent with NIR profiles in both hemispheres. The increase in water to 100 ppmv below 30–40 km in the Northern Hemisphere repeats in all years, with some temporal and spatial variations. Both SPICAM and ACS NIR have shown an increase in the saturation ratio above 30–40 km, where the water v.m.r. sharply decreases to a few ppmvs. A strong high-latitude supersaturation detected by NIR in the Southern Hemisphere below 20 km (MY34-35) is supported by SPICAM in MY29 at $L_s \sim 80°$, where latitudes ~60°S were observed. Concluding, SPICAM and ACS NIR observations of H_2O saturation state are generally in good agreement.

On the contrary, Poncin et al. (2022) did not find evidence for large or widespread supersaturation in the Martian atmosphere. From CRISM analysis, they conclude that during the aphelion season, the atmospheric water is close to saturation when clouds are present and can reach a supersaturation ratio of 2–3 at most at 10–50 km. During the dusty season, subsaturation was prevalent, in agreement with a previous CRISM study by Clancy et al. (2017). Also, a comparison of NOMAD water profiles and MCS atmospheric temperatures made by Poncin et al. (2022) during the GDS decay and the "C" storm of MY34 has shown one case of saturation ratio reaching 5 at the top of the cloud layer and below 2 in other cases. These results were more in line with the traditional understanding that water vapor is close to saturation in the presence of water ice clouds. However, the analyzed water-temperature combinations from the CRISM-MCS or NOMAD-MCS data sets were not completely simultaneous. Still, our results and those of Poncin et al. (2022) do not contradict each other. As shown in Figure 11, the water vapor mixing ratio and its saturation state is very dynamic and changes dramatically from occultation to occultation with latitude and L_s not only in the dusty season presented in Fedorova et al. (2020) but in the aphelion season as well.

Solar occultation observations at the terminator reflect transient conditions between day and night where a strong temperature contrast can stimulate fast processes. Connour et al. (2020) have reported twilight cloud bands routinely forming past the evening terminator (18:00–19:00 local time) during the MY 34 GDS as a result of rapidly changing temperatures. The cloud bands in the IUVS/MAVEN images were often latitudinally continuous, spanning over 6,000 km and reaching 40–50 km altitudes. Such clouds were also detected in the ACS observations during GDS (Fedorova et al., 2020; Liuzzi et al., 2020; Luginin et al., 2020; Stcherbinine et al., 2020), together with strong lifting of supersaturated water. The morning-to-evening difference in the saturation state observed by ACS (Figure 10) supports the idea that supersaturation cases can be related to semidiurnal thermal tides in the atmosphere.

The recent study of the MY34 GDS with Mars Assimilated Remote Soundings (OpenMars) data set of the Mars GCM group in the Open University (Holmes et al., 2022) has shown that discrete layers of supersaturation above 60 km exist across all latitudes during the MY34 dusty season with the diurnal variation in the saturation state of the atmosphere. This is consistent with the ACS NIR observations not only for MY34 but also for MY35. Holmes et al. (2022) also found evidence of supersaturated water vapor breaking into the northern winter polar vortex. The supersaturated layer centered roughly at 40 km exists at latitudes poleward of 60°N that corresponds to the cold air below the polar warming at high northern latitudes and can be extended down below 20 km during polar winter. In MY34, ACS NIR observed high northern latitudes at L_s = 180°–210° and 330°–360°, and supersaturation was found only within the last bin at the end of the year. At L_s = 180°–210°, water was saturated in polar latitudes, but the saturation ratio did not exceed 3. In MY35, the coverage was better, and the supersaturated layer was observed at L_s = 180°–240° and 300°–360° in high latitudes. The difference with model results is related to the altitude of the supersaturated layer: for ACS observation it is located below 30 km for both MY34 and MY35, whereas the water assimilation model shows it is 10 km higher. In any case, the general consistency of the assimilation and observations gives a promising perspective for water vapor saturation modeling.

On Earth, the cold trap above the tropopause works well to stop water vapor and make the stratosphere extremely dry (Lunine & Hunten, 1989). However, the supersaturated water also happens on Earth, but in extremely cold conditions. Polar mesospheric clouds (PMCs) are water ice clouds occurring in the terrestrial atmosphere at about 83–90 km altitude near the mesopause during the polar summer (Duft et al., 2019). The mean temperature in this region is about 140 K that makes it close to Mars. A typical H_2O volume mixing ratio of about a few ppmvs leads to strong supersaturation (Hervig et al., 2009; Lübken et al., 2009). It was assumed that these clouds are crystalline ice formed by heterogeneous nucleation of meteoric smoke particles ablated from meteoroids in the upper atmosphere (Gumbel & Megner, 2009). The recent laboratory measurements supported that ice growth on such particles with radius ≥1 nm initiates with S ∼10–50, a value which is commonly exceeded during the season of PMCs (Duft et al., 2019). The high-altitude cirrus clouds in the stratosphere were also found with water vapor in a supersaturated state up to 50% in ultracold conditions (<200 K). One explanation invokes the formation of amorphous solid water (ASW) at temperatures below 160 K, whose vapor pressure exceeds that of hexagonal ice and can reach 5–10 at low temperatures (Nachbar et al., 2019). ASW is metastable and converts to crystalline or nano-crystalline ice above about 130 K, for which the saturation vapor pressure is 100%–200% higher compared to stable hexagonal ice (Nachbar et al., 2018). Even after an ice crystal has transformed into hexagonal ice, surface effects might hinder its growth (Peter et al., 2006).

In this case, the Mars cold atmosphere could reflect the extreme cases of PMCs and stratospheric clouds combined with different reasons for the often presence of supersaturation-like formation of ASW and metastable ices (Mangan et al., 2021), absence or submicron-sized ice condensation nucleus in the upper atmosphere, or/and fast upward/downward flows compared to timescales of relaxation to saturation.

5. Conclusions

We analyzed a two-Mars Year data set of H_2O profiles consisting of solar occultation observations by ACS NIR. The data were collected from April 2018 (L_s = 163° of MY 34) to January 2022 (L_s = 170° of MY 36) and contain about 8,500 water vertical profiles with simultaneous retrieval of CO_2 density and temperature. The latter was obtained from 1.43 μm and 1.65 μm CO_2 bands (orders 49 and 54 of the spectrometer) in the range of altitudes from 0 to 110 km and the H_2O mixing ratio in the 1.38 μm water band (order 56 of the spectrometer) in the range of altitudes from 0 to 100 km. To provide a comparison with aerosol loading, we used the aerosol extinction at

1.4 μm from the same ACS NIR observations and H_2O ice extinction from simultaneous ACS MIR observation at 3.3 μm H_2O ice band.

With this data set, we have presented the first detailed analysis of the vertical distribution of the water vapor saturation state. Using our data set, we studied the seasonal, latitudinal and local time variations and found the following:

1. We confirm previous observations (Alday et al., 2021; Fedorova et al., 2021) that water vertical distribution is variable with season and reaches 100 km in the perihelion and 60 km in the aphelion season. The simultaneous measurement of atmospheric temperature allows us to calculate the saturation state of water vapor and the presence of supersaturation was found to be nearly ubiquitous above aerosol layers. This finding implies that water escape processes rely on complex interactions between thermodynamics, dynamics, chemistry and microphysics that only fully coupled climate models can address.
2. In the aphelion season, the water mixing ratio above 40 km in the mid-to-high latitudes is observed to be lower than 3 ppmv and is found to be supersaturated in low-to-mid latitudes from $L_s = 0°$ to 180°. Also, supersaturation was found in southern and northern polar regions below 20–30 km close to both equinoxes, correlating the region where water vapor transported from low latitudes meets the cold polar vortex.
3. Around the perihelion, water is also supersaturated with a mixing ratio of 30–50 ppmv that is typical of altitudes above 60 km. Stronger saturation is observed during the dusty season in MY35 compared to what was observed in MY34 during the GDS and around the perihelion. In the dusty season, the polar maximum of supersaturation at 20 km is present in both hemispheres and the most prominent close to equinoxes.
4. Water vapor abundance and its saturation state were found to vary between the evening and morning terminators in response to temperature modulation imparted by thermal tides. Although water vapor is found to be more abundant in the evening, colder temperatures observed in the morning induce a daily peak of saturation.
5. The observations at $L_s = 50°–120°$ during the aphelion season of MY34 and MY35 have shown a good consistency with SPICAM IR observations on Mars-Express in MY29 that demonstrates that supersaturation is a repeatable state of water vapor in the Martian atmosphere from year to year.

In prospect, the microphysical modeling at low temperatures combined with the circulation modeling will be needed to explain the extreme saturation state of water on Mars. But if very low temperature in the middle and upper atmosphere is a reason for frequent supersaturation, the current Martian climate even facilitates the water escape to space.

Data Availability Statement

ACS data are available from ESA Planetary Science Archive (PSA) Level 2 (https://archives.esac.esa.int/psa/#!Table%20View/ACS=instrument). The H_2O, temperature, and saturation coefficient vertical profiles generated from ACS-NIR measurements and analyzed in this study are available at Fedorova (2022).

Acknowledgments
The ExoMars mission is a joint mission of the European Space Agency (ESA) and Roscosmos. The ACS experiment is led by the Space Research Institute (IKI) in Moscow, assisted by LATMOS in France. The science operations of ACS are funded by the Roscosmos and ESA. The authors affiliated with IKI acknowledge funding from the Ministry of Science and Higher Education of the Russian Federation (subsidies, theme "Planeta"). The authors affiliated with LATMOS acknowledge funding from the Centre National d'Etudes Spatiales (CNES) and the Centre National de la Recherche Scientifique (CNRS).

References

Alday, J., Trokhimovskiy, A., Irwin, P. G. J., Wilson, C. F., Montmessin, F., Lefévre, F., et al. (2021). Isotopic fractionation of water and its photolytic products in the atmosphere of Mars. *Nature Astronomy*, *5*(9), 943–950. https://doi.org/10.1038/s41550-021-01389-x

Alday, J., Wilson, C. F., Irwin, P. G. J., Olsen, K. S., Baggio, L., Montmessin, F., et al. (2019). Oxygen isotopic ratios in Martian water vapour observed by ACS MIR on board the ExoMars Trace Gas Orbiter. *A&A*, *630*, A91. https://doi.org/10.1051/0004-6361/201936234

Aoki, S., Vandaele, A. C., Daerden, F., Villanueva, G. L., Liuzzi, G., Clancy, R. T., et al. (2022). Global vertical distribution of water vapor on Mars: Results from 3.5 years of ExoMars-TGO/NOMAD science operations. *Journal of Geophysical Research: Planets*, *127*(9), 2022JE007231. https://doi.org/10.1029/2022je007231

Aoki, S., Vandaele, A. C., Daerden, F., Villanueva, G. L., Liuzzi, G., Thomas, I. R., et al. (2019). Water vapor vertical profiles on Mars in dust storms observed by TGO/NOMAD. *Journal of Geophysical Research: Planets*, *124*(12), 3482–3497. https://doi.org/10.1029/2019je006109

Belyaev, D. A., Fedorova, A. A., Trokhimovskiy, A., Alday, J., Montmessin, F., Korablev, O. I., et al. (2021). Revealing a high water abundance in the upper mesosphere of Mars with ACS onboard TGO. *Geophysical Research Letters*, *48*(10), e93411. https://doi.org/10.1029/2021GL093411

Ceccherini, S. (2005). Analytical determination of the regularization parameter in the retrieval of atmospheric vertical profiles. *Optics Letters*, *30*(19), 2554–2556. https://doi.org/10.1364/ol.30.002554

Ceccherini, S., Belotti, C., Carli, B., Raspollini, P., & Ridolfi, M. (2007). Technical Note: Regularization performances with the error consistency method in the case of retrieved atmospheric profiles. *Atmospheric Chemistry and Physics*, *7*(5), 1435–1440. https://doi.org/10.5194/acp-7-1435-2007

Chaffin, M. S., Chaufray, J.-Y., Stewart, I., Montmessin, F., Schneider, N. M., & Bertaux, J.-L. (2014). Unexpected variability of Martian hydrogen escape. *Geophysical Research Letters*, *41*(2), 314–320. https://doi.org/10.1002/2013GL058578

Chaffin, M. S., Deighan, J., Schneider, N. M., & Stewart, A. I. F. (2017). Elevated atmospheric escape of atomic hydrogen from Mars induced by high-altitude water. *Nature Geoscience*, *10*(3), 174–178. https://doi.org/10.1038/ngeo2887

Chaffin, M. S., Kass, D. M., Aoki, S., Fedorova, A. A., Deighan, J., Connour, K., et al. (2021). Martian water loss to space enhanced by regional dust storms. *Nature Astronomy*, *5*(10), 1036–1042. https://doi.org/10.1038/s41550-021-01425-w

Clancy, R. T., Grossman, A. W., Wolff, M. J., James, P. B., Rudy, D. J., Billawala, Y. N., et al. (1996). Water vapor saturation at low altitudes around Mars aphelion: A key to Mars climate? *Icarus*, *122*(1), 36–62. https://doi.org/10.1006/icar.1996.0108

Clancy, R. T., Smith, M. D., Lefèvre, F., McConnochie, T. H., Sandor, B. J., Wolff, M., et al. (2017). Vertical profiles of Mars 1.27 μm O_2 dayglow from MRO CRISM limb spectra: Seasonal/global behaviors, comparisons to LMD GCM simulations, and a global definition for Mars water vapor profiles. *Icarus*, *293*, 132–156. https://doi.org/10.1016/j.icarus.2017.04.011

Clarke, J. T., Bertaux, J. L., Chaufray, J. Y., Gladstone, G. R., Quemerais, E., Wilson, J. K., & Bhattacharyya, D. (2014). A rapid decrease of the hydrogen corona of Mars. *Geophysical Research Letters*, *41*(22), 8013–8020. https://doi.org/10.1002/2014GL061803

Connour, K., Schneider, N. M., Milby, Z., Forget, F., Alhosani, M., Spiga, A., et al. (2020). Mars's twilight cloud band: A new cloud feature seen during the Mars Year 34 global dust storm. *Geophysical Research Letters*, *47*(1), e2019GL084997. https://doi.org/10.1029/2019GL084997

Duft, D., Nachbar, M., & Leisner, T. (2019). Unravelling the microphysics of polar mesospheric cloud formation. *Atmospheric Chemistry and Physics*, *19*(5), 2871–2879. https://doi.org/10.5194/acp-19-2871-2019

Fedorova, A. (2022). Water vapor saturation state on Mars from ACS-NIR/TGO occultations from MY34 to MY36. Mendeley Data, V1. https://doi.org/10.17632/6xrn9v4dc5.1

Fedorova, A., Bertaux, J. L., Betsis, D., Montmessin, F., Korablev, O., Maltagliati, L., & Clarke, J. (2018). Water vapor in the middle atmosphere of Mars during the 2007 global dust storm. *Icarus*, *300*, 440–457. https://doi.org/10.1016/j.icarus.2017.09.025

Fedorova, A., Montmessin, F., Korablev, O., Lefèvre, F., Trokhimovskiy, A., & Bertaux, J.-L. (2021). Multi-annual monitoring of the water vapor vertical distribution on Mars by SPICAM on Mars Express. *Journal of Geophysical Research: Planets*, *126*(1), e2020JE006616. https://doi.org/10.1029/2020JE006616

Fedorova, A., Trokhimovskiy, A., Lefèvre, F., Olsen, K. S., Korablev, O., Montmessin, F., et al. (2022). Climatology of the CO vertical distribution on Mars based on ACS TGO measurements. *Journal of Geophysical Research: Planets*, *127*(9), e2022JE007195. https://doi.org/10.1029/2022JE007195

Fedorova, A. A., Korablev, O. I., Bertaux, J. L., Rodin, A. V., Montmessin, F., Belyaev, D. A., & Reberac, A. (2009). Solar infrared occultation observations by SPICAM experiment on Mars-Express: Simultaneous measurements of the vertical distributions of H_2O, CO_2 and aerosol. *Icarus*, *200*(1), 96–117. https://doi.org/10.1016/j.icarus.2008.11.006

Fedorova, A. A., Montmessin, F., Korablev, O., Luginin, M., Trokhimovskiy, A., Belyaev, D. A., et al. (2020). Stormy water on Mars: The distribution and saturation of atmospheric water during the dusty season. *Science*, *367*(6475), 297–300. https://doi.org/10.1126/science.aay9522

Fedorova, A. A., Montmessin, F., Rodin, A. V., Korablev, O. I., Määttänen, A., Maltagliati, L., & Bertaux, J. L. (2014). Evidence for a bimodal size distribution for the suspended aerosol particles on Mars. *Icarus*, *231*(0), 239–260. https://doi.org/10.1016/j.icarus.2013.12.015

Forbes, J. M., Zhang, X., Forget, F., Millour, E., & Kleinböhl, A. (2020). Solar tides in the middle and upper atmosphere of Mars. *Journal of Geophysical Research: Space Physics*, *125*(9), e2020JA028140. https://doi.org/10.1029/2020JA028140

Gamache, R. R., Neshyba, S., Plateaux, J., Barbe, A., Regalia, L., & Pollack, J. (1995). CO_2-broadening of water-vapor lines. *Journal of Molecular Spectroscopy*, *170*(1), 131–151. https://doi.org/10.1006/jmsp.1995.1060

Giuranna, M., Wolkenberg, P., Grassi, D., Aronica, A., Aoki, S., Scaccabarozzi, D., et al. (2021). The current weather and climate of Mars: 12 years of atmospheric monitoring by the planetary Fourier spectrometer on Mars Express. *From Mars Express to Exomars*, *353*, 113406. https://doi.org/10.1016/j.icarus.2019.113406

Goff, J. A., & Gratch, S. (1946). Low-pressure properties of water from −160 to 212 F. *Transactions of the American Society of Heating and Ventilating Engineers*, 25–164.

Gordon, I. E., Rothman, L. S., Hill, C., Kochanov, R. V., Tan, Y., Bernath, P. F., et al. (2017). The HITRAN2016 molecular spectroscopic database. *Journal of Quantitative Spectroscopy & Radiative Transfer*, *203*, 3–69. https://doi.org/10.1016/j.jqsrt.2017.06.038

Guerlet, S., Ignatiev, N., Forget, F., Fouchet, T., Vlasov, P., Bergeron, G., et al. (2022). Thermal structure and aerosols in Mars' atmosphere from TIRVIM/ACS onboard the ExoMars Trace Gas Orbiter: Validation of the retrieval algorithm. *Journal of Geophysical Research: Planets*, *127*, 2. https://doi.org/10.1029/2021je007062

Gumbel, J., & Megner, L. (2009). Charged meteoric smoke as ice nuclei in the mesosphere: Part 1—A review of basic concepts. *Journal of Atmospheric and Solar-Terrestrial Physics*, *71*(12), 1225–1235. https://doi.org/10.1016/j.jastp.2009.04.012

Haberle, R. M., Joshi, M. M., Murphy, J. R., Barnes, J. R., Schofield, J. T., Wilson, G., et al. (1999). General circulation model simulations of the Mars Pathfinder atmospheric structure investigation/meteorology data. *Journal of Geophysical Research*, *104*(E4), 8957–8974. https://doi.org/10.1029/1998JE900040

Haberle, R. M., Kahre, M. A., Hollingsworth, J. L., Montmessin, F., Wilson, R. J., Urata, R. A., et al. (2019). Documentation of the NASA/Ames Legacy Mars global climate model: Simulations of the present seasonal water cycle. *Icarus*, *333*, 130–164. https://doi.org/10.1016/j.icarus.2019.03.026

Heavens, N. G., Kleinböhl, A., Chaffin, M. S., Halekas, J. S., Kass, D. M., Hayne, P. O., et al. (2018). Hydrogen escape from Mars enhanced by deep convection in dust storms. *Nature Astronomy*, *2*(2), 126–132. https://doi.org/10.1038/s41550-017-0353-4

Heavens, N. G., McCleese, D. J., Richardson, M. I., Kass, D. M., Kleinböhl, A., & Schofield, J. T. (2011). Structure and dynamics of the Martian lower and middle atmosphere as observed by the Mars climate sounder: 2. Implications of the thermal structure and aerosol distributions for the mean meridional circulation. *Journal of Geophysical Research*, *116*(E1), E01010. https://doi.org/10.1029/2010JE003713

Hervig, M. E., Stevens, M. H., Gordley, L. L., Deaver, L. E., Russell, J. M., & Bailey, S. M. (2009). Relationships between polar mesospheric clouds, temperature, and water vapor from Solar Occultation for Ice Experiment (SOFIE) observations. *Journal of Geophysical Research*, *114*(D20), D20203. https://doi.org/10.1029/2009JD012302

Holmes, J. A., Lewis, S. R., Patel, M. R., Alday, J., Aoki, S., Liuzzi, G., et al. (2022). Global variations in water vapour and saturation state throughout the Mars Year 34 dusty season. *Journal of Geophysical Research: Planets*, *127*(10), e2022JE007203. https://doi.org/10.1029/2022JE007203

Holmes, J. A., Lewis, S. R., Patel, M. R., Chaffin, M. S., Cangi, E. M., Deighan, J., et al. (2021). Enhanced water loss from the Martian atmosphere during a regional-scale dust storm and implications for long-term water loss. *Earth and Planetary Science Letters*, *571*, 117109. https://doi.org/10.1016/j.epsl.2021.117109

Houben, H., Haberle, R. M., Young, R. E., & Zent, A. P. (1997). Modeling the Martian seasonal water cycle. *Journal of Geophysical Research*, *102*(E4), 9069–9083. https://doi.org/10.1029/97je00046

Huang, J. (2018). A simple accurate formula for calculating saturation vapor pressure of water and ice. *Journal of Applied Meteorology and Climatology*, *57*(6), 1265–1272. https://doi.org/10.1175/jamc-d-17-0334.1

Kass, D. M., Kleinböhl, A., McCleese, D. J., Schofield, J. T., & Smith, M. D. (2016). Interannual similarity in the Martian atmosphere during the dust storm season. *Geophysical Research Letters*, *43*(12), 6111–6118. https://doi.org/10.1002/2016GL068978

Kass, D. M., Schofield, J. T., Kleinböhl, A., McCleese, D. J., Heavens, N. G., Shirley, J. H., & Steele, L. J. (2020). Mars Climate Sounder observation of Mars' 2018 global dust storm. *Geophysical Research Letters*, *47*(23), e2019GL083931. https://doi.org/10.1029/2019GL083931

Kleinböhl, A., John Wilson, R., Kass, D., Schofield, J. T., & McCleese, D. J. (2013). The semidiurnal tide in the middle atmosphere of Mars. *Geophysical Research Letters*, *40*(10), 1952–1959. https://doi.org/10.1002/grl.50497

Kleinböhl, A., Spiga, A., Kass, D. M., Shirley, J. H., Millour, E., Montabone, L., & Forget, F. (2020). Diurnal variations of dust during the 2018 global dust storm observed by the Mars climate sounder. *Journal of Geophysical Research: Planets*, *125*(1), e2019JE006115. https://doi.org/10.1029/2019JE006115

Korablev, O., Montmessin, F., Trokhimovskiy, A., Fedorova, A. A., Shakun, A. V., Grigoriev, A. V., et al. (2018). The Atmospheric Chemistry Suite (ACS) of three spectrometers for the ExoMars 2016 Trace Gas Orbiter. *Space Science Reviews*, *214*(1), 7. https://doi.org/10.1007/s11214-017-0437-6

Krasnopolsky, V. A. (2019). Photochemistry of water in the Martian thermosphere and its effect on hydrogen escape. *Icarus*, *321*, 62–70. https://doi.org/10.1016/j.icarus.2018.10.033

List, R. J. (1984). *Smithsonian Institution, Smithsonian meteorological tables*. Smithsonian Institution Press.

Liuzzi, G., Villanueva, G. L., Crismani, M. M. J., Smith, M. D., Mumma, M. J., Daerden, F., et al. (2020). Strong variability of Martian water ice clouds during dust storms revealed from ExoMars Trace Gas Orbiter/NOMAD. *Journal of Geophysical Research: Planets*, *125*(4), e2019JE006250. https://doi.org/10.1029/2019JE006250

Lübken, F.-J., Lautenbach, J., Höffner, J., Rapp, M., & Zecha, M. (2009). First continuous temperature measurements within polar mesosphere summer echoes. *Global Perspectives on the Aeronomy of the Summer Mesopause Region*, *71*(3), 453–463. https://doi.org/10.1016/j.jastp.2008.06.001

Luginin, M., Fedorova, A., Ignatiev, N., Trokhimovskiy, A., Shakun, A., Grigoriev, A., et al. (2020). Properties of water ice and dust particles in the atmosphere of Mars during the 2018 global dust storm as inferred from the Atmospheric Chemistry Suite. *Journal of Geophysical Research: Planets*, *125*(11), 1–22. https://doi.org/10.1029/2020JE006419

Lunine, J. I., & Hunten, D. M. (1989). Abundance of condensable species at planetary cold traps: The role of moist convection. *Planetary and Space Science*, *37*(2), 151–166. https://doi.org/10.1016/0032-0633(89)90003-2

Madeleine, J.-B., Forget, F., Millour, E., Navarro, T., & Spiga, A. (2012). The influence of radiatively active water ice clouds on the Martian climate. *Geophysical Research Letters*, *39*(23), L23202. https://doi.org/10.1029/2012GL053564

Maltagliati, L., Montmessin, F., Fedorova, A., Korablev, O., Forget, F., & Bertaux, J.-L. (2011). Evidence of water vapor in excess of saturation in the atmosphere of Mars. *Science*, *333*(6051), 1868–1871. https://doi.org/10.1126/science.1207957

Maltagliati, L., Montmessin, F., Korablev, O., Fedorova, A., Forget, F., Määttänen, A., et al. (2013). Annual survey of water vapor vertical distribution and water–aerosol coupling in the Martian atmosphere observed by SPICAM/MEx solar occultations. *Icarus*, *223*(2), 942–962. https://doi.org/10.1016/j.icarus.2012.12.012

Mangan, T. P., Plane, J. M. C., & Murray, B. J. (2021). The phase of water ice which forms in cold clouds in the mesospheres of Mars, Venus, and Earth. *Journal of Geophysical Research: Planets*, *126*(3), e2020JE006796. https://doi.org/10.1029/2020JE006796

Montmessin, F., Belyaev, D. A., Lefèvre, F., Alday, J., Vals, M., Fedorova, A. A., et al. (2022). Reappraising the production and transfer of hydrogen atoms from the middle to the upper atmosphere of Mars at times of elevated water vapor. *Journal of Geophysical Research: Planets*, *127*(5), e07217. https://doi.org/10.1029/2022JE007217

Montmessin, F., Forget, F., Rannou, P., Cabane, M., & Haberle, R. M. (2004). Origin and role of water ice clouds in the Martian water cycle as inferred from a general circulation model. *Journal of Geophysical Research*, *109*(E10), E10004. https://doi.org/10.1029/2004je002284

Nachbar, M., Duft, D., & Leisner, T. (2018). The vapor pressure over nano-crystalline ice. *Atmospheric Chemistry and Physics*, *18*(5), 3419–3431. https://doi.org/10.5194/acp-18-3419-2018

Nachbar, M., Duft, D., & Leisner, T. (2019). The vapor pressure of liquid and solid water phases at conditions relevant to the atmosphere. *The Journal of Chemical Physics*, *151*(6), 064504. https://doi.org/10.1063/1.5100364

Navarro, T., Madeleine, J.-B., Forget, F., Spiga, A., Millour, E., Montmessin, F., & Määttänen, A. (2014). Global climate modeling of the Martian water cycle with improved microphysics and radiatively active water ice clouds. *Journal of Geophysical Research: Planets*, *119*(7), 1479–1495. https://doi.org/10.1002/2013JE004550

Neary, L., Daerden, F., Aoki, S., Whiteway, J., Clancy, R. T., Smith, M., et al. (2020). Explanation for the increase in high-altitude water on Mars observed by NOMAD during the 2018 global dust storm. *Geophysical Research Letters*, *47*(7), e2019GL084354. https://doi.org/10.1029/2019gl084354

Peter, T., Marcolli, C., Spichtinger, P., Corti, T., Baker, M. B., & Koop, T. (2006). When dry air is too humid. *Science*, *314*(5804), 1399–1402. https://doi.org/10.1126/science.1135199

Poncin, L., Kleinböhl, A., Kass, D. M., Clancy, R. T., Aoki, S., & Vandaele, A. C. (2022). Water vapor saturation and ice cloud occurrence in the atmosphere of Mars. *Planetary and Space Science*, *212*, 105390. https://doi.org/10.1016/j.pss.2021.105390

Richardson, M. I., & Wilson, R. J. (2002a). Investigation of the nature and stability of the Martian seasonal water cycle with a general circulation model. *Journal of Geophysical Research: Planets*, *107*(E5), 5031. https://doi.org/10.1029/2001JE001536

Richardson, M. I., & Wilson, R. J. (2002b). A topographically forced asymmetry in the Martian circulation and climate. *Nature*, *416*(6878), 298–301. https://doi.org/10.1038/416298a

Rodgers, C. D. (2000). *Inverse methods for atmospheric sounding: Theory and practice*. World Scientific.

Shaposhnikov, D. S., Medvedev, A. S., Rodin, A. V., Yiğit, E., & Hartogh, P. (2022). Martian dust storms and gravity waves: Disentangling water transport to the upper atmosphere. *Journal of Geophysical Research: Planets*, *127*(1), e2021JE007102. https://doi.org/10.1029/2021JE007102

Shaposhnikov, D. S., Medvedev, A. S., Rodin, A. V. V., & Hartogh, P. (2019). Seasonal water "pump" in the atmosphere of Mars: Vertical transport to the thermosphere. *Geophysical Research Letters*, *46*(8), 4161–4169. https://doi.org/10.1029/2019GL082839

Stcherbinine, A., Vincendon, M., Montmessin, F., Wolff, M. J., Korablev, O., Fedorova, A., et al. (2020). Martian water ice clouds during the 2018 global dust storm as observed by the ACS mid-infrared channel onboard the Trace Gas Orbiter. *Journal of Geophysical Research: Planets*, *125*(3), e2019JE006300. https://doi.org/10.1029/2019JE006300

Stone, S. W., Yelle, R. V., Benna, M., Lo, D. Y., Elrod, M. K., & Mahaffy, P. R. (2020). Hydrogen escape from Mars is driven by seasonal and dust storm transport of water. *Science*, *370*(6518), 824–831. https://doi.org/10.1126/science.aba5229

Trokhimovskiy, A., Fedorova, A., Korablev, O., Montmessin, F., Bertaux, J.-L., Rodin, A., & Smith, M. D. (2015). Mars' water vapor mapping by the SPICAM IR spectrometer: Five Martian years of observations. *Icarus*, *251*, 50–64. https://doi.org/10.1016/j.icarus.2014.10.007

Trokhimovskiy, A., Korablev, O., Kalinnikov, Y. K., Fedorova, A., Stepanov, A. V., Titov, A. Y., et al. (2015). Near-infrared echelle-AOTF spectrometer ACS-NIR for the ExoMars Trace Gas Orbiter. In *Infrared remote sensing and instrumentation XXIII* (Vol. 9608, pp. 62–70). SPIE. https://doi.org/10.1117/12.2190369

Vals, M., Rossi, L., Montmessin, F., Lefèvre, F., Gonzalez-Galindo, F., Fedorova, A., et al. (2022). Improved modeling of Mars' HDO cycle using a Mars' global climate model. *Journal of Geophysical Research: Planets*, *127*(8), e2022JE007192. https://doi.org/10.1029/2022JE007192

Villanueva, G. L., Liuzzi, G., Crismani, M. M. J., Aoki, S., Vandaele, A. C., Daerden, F., et al. (2021). Water heavily fractionated as it ascends on Mars as revealed by ExoMars/NOMAD. *Science Advances*, *7*, eabc8843. https://doi.org/10.1126/sciadv.abc8843

Wagner, W., Riethmann, T., Feistel, R., & Harvey, A. H. (2011). New equations for the sublimation pressure and melting pressure of H_2O ice Ih. *Journal of Physical and Chemical Reference Data*, *40*(4), 043103. https://doi.org/10.1063/1.3657937

Wilson, R. J. (2000). Evidence for diurnal period Kelvin waves in the Martian atmosphere from Mars Global Surveyor TES data. *Geophysical Research Letters*, *27*(23), 3889–3892. https://doi.org/10.1029/2000GL012028

Wolkenberg, P., & Giuranna, M. (2021). Daily dust variation from the PFS MEx observations. *From Mars Express to Exomars*, *353*, 113823. https://doi.org/10.1016/j.icarus.2020.113823

Wu, Z., Li, T., & Dou, X. (2015). Seasonal variation of Martian middle atmosphere tides observed by the Mars Climate Sounder. *Journal of Geophysical Research: Planets*, *120*(12), 2206–2223. https://doi.org/10.1002/2015JE004922

Zurek, R. W. (1976). Diurnal tide in the Martian atmosphere. *Journal of Atmospheric Sciences*, *33*(2), 321–337. https://doi.org/10.1175/1520-0469(1976)033<0321:dtitma>2.0.co;2